UNIVERSITY OF THESSALY

SCHOOL OF ENGINEERING

DEPARTMENT OF MECHANICAL ENGINEERING

# MECHANICAL BEHAVIOR OF BRACE-TO-CYLINDER WELDED STIFFENED CONNECTIONS IN TLP WIND ENERGY PLATFORMS

by

**GEORGIOS T. PLAKIAS**

Submitted in partial fulfillment of the requirements for the degree of Diploma
in Mechanical Engineering at the University of Thessaly

Volos, 2021

**Approved by the Committee on Final Examination:**


Advisor           Dr. Spyridon A. Karamanos,

Professor, Department of Mechanical Engineering,

University of Thessaly


Member          Dr. Anna Zervaki,

Ass. Professor, School of Naval Architecture and Marine Engineering,

Division of Marine Structures, Shipbuilding Technology Laboratory (STL),

National Technical University of Athens (NTUA)


Member          Dr. Gregory N. Haidemenopoulos,

Professor, Department of Mechanical Engineering,

University of Thessaly


Date Approved:  October 11, 2021

# MECHANICAL BEHAVIOR OF BRACE-TO-CYLINDER WELDED STIFFENED CONNECTIONS IN TLP WIND ENERGY PLATFORMS

Georgios T. Plakias

Department of Mechanical Engineering, University of Thessaly

Supervisor: Dr. Spyridon A. Karamanos

Professor of Numerical Methods – Finite Elements - Structural Mechanics

**Abstract**

Offshore wind energy is rapidly developing, motivated by the stronger and more regular winds at sea with respect to land areas. The present thesis is part of a European research program (REFOS, 2016-2019), which aimed at the development of a deep-water offshore multi-purpose floating system suitable for producing simultaneously wind and wave energy.

The system consists of a triangular platform supported by cylindrical floaters with the wind turbine mounted at the deck center (Central Floater - CF) and the cylindrical OWC devices at its three corners (Peripheral floaters - PF). Floaters consist of an external thin skin, reinforced with vertical and horizontal stiffness in the inner side. Peripheral and Central Floaters are connected with each other with a set of braces, welded on the outer side of the floaters' skin. In a previous elementary study, a numerical model was developed, which included the whole platform. The results showed that the weakest points of the structure lie in the weld-ed connection between the Peripheral Floaters and the Brace.

The thesis is presenting a detailed numerical model of the region around the connection of the brace with the skin, including the weldment and the inner stiffeners. The model was developed in the general-purpose finite element software Abaqus. The model was validated using experimental data from the response force of the hydraulic actuator. The connection is analyzed in fatigue and ultimate monotonic loading. Regarding the mechanical behavior in fatigue, the Stress Concentration Factor (SCF) is computed, the influence of stiffeners on local deformation is investigated, and critical regions are identified in terms of local stresses. Besides that, the ultimate capacity of the connection is calculated.

According to the observations and results, two alternative designs are proposed and analyzed in similar conditions as the initial design. Finally, modelling suggestions are presented for more detailed analysis of the alternative designs.

**Key words:** Floating Offshore Energy, Finite Elements Analysis, Brace – Cylinder Connection

# Contents

# 1 Offshore wind energy

In this chapter some of the fundamental information about offshore wind power will be presented, to allow the reader understand the subsequent chapters. The main concepts of offshore wind energy will be described and then the floating offshore supporting structures will be presented.

## 1.1 Offshore Wind – A Brief History

Europe is the world leader in offshore wind power, with the first offshore wind farm (Vindeby) being installed in Denmark in 1991. In 2009, the average nameplate capacity of an offshore wind turbine in Europe was about 3 MW, and the capacity of future turbines was expected to increase to 5 MW. In 2013, offshore wind power contributed to 1,567 MW of the total 11,159 MW of wind power capacity constructed that year. By January 2014, 69 offshore wind farms had been constructed in Europe with an average annual rated capacity of 482 MW. The total installed capacity of offshore wind farms in European waters reached 6,562 MW.



*Figure 1: Built in 1991, Vindeby in Denmark was the world's first offshore wind farm*

The United Kingdom has by far the largest capacity with 3,681 MW. Denmark is second with 1,271 MW installed and Belgium was third with 571 MW. Germany comes fourth with 520 MW, followed by the Netherlands (247 MW), Sweden (212 MW), Finland (26 MW), Ireland (25 MW), Spain (5 MW), Norway (2 MW) and Portugal (2 MW).

At the end of 2015, 3,230 turbines at 84 offshore wind farms across 11 European countries had been installed and grid-connected, making a total capacity of 11,027 MW. At its maximum potential, offshore wind production could reach more than 120,000 gigawatts (GW), or 11 times the projected global electricity demand in 2040.
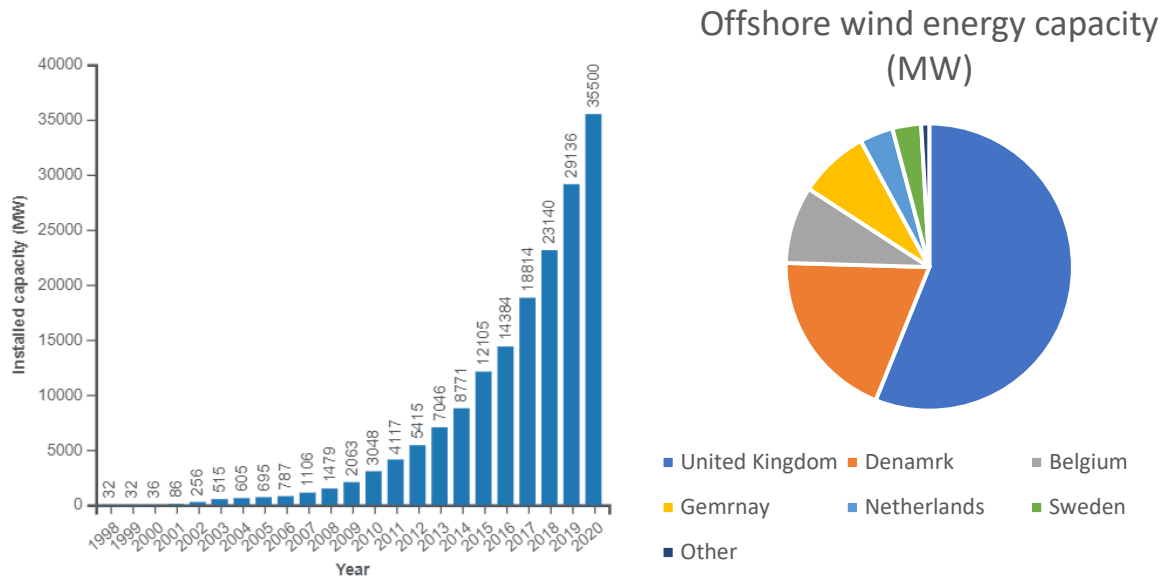
*Figure 2: Wind energy capacity through from 1998 to 2020 around the world (left), Offshore wind energy distribution in different countries for year 2020 (right)*

### 1.1.1    Wind energy in Greece

Currently Greece has 4 GW of wind energy installed, all onshore, covering 12% of its electricity demand.  But the potential for wind energy in Greece is much bigger, especially for offshore wind. The deep waters in Greek seas dictate the implementation of floating wind for exploiting the offshore wind resources.

Costs for bottom-fixed turbines are higher in deeper waters, such as in the Mediterranean, but floating wind offers new perspectives.  There are currently 62 MW of floating offshore wind in Europe, including the 30 MW Hywind wind farm in Scotland and the 25 MW WindFloat Atlantic wind farm in Portugal, now fully operational.  Europe's "pipeline" of floating offshore projects is worth over 7 GW for the next decade.

## 1.2    Main Parts of Wind Turbines

Wind turbines consist of the following main parts:

- Rotor
- Drive train
- Nacelle
- Tower
- Support structure, including its foundation

The **rotor** includes the blades and the hub, which join the blades together and connect them to a shaft. Most modern wind turbines are of horizontal-axis type and have three blades. The blades are usually made of composites and constitutes a big part of the cost for a new turbine.

The **drive train**, in addition to the rotor, consist the rotating parts of the turbine. It often consists of shafts, a gearbox, couplings, a brake system and the generator for generating electricity. The rotor turns with a low rpm, usually less than 10 rpm for a large rotor, while the generators operate with higher frequency. This is the reason for having a gearbox which transfers the slow rotational speed of the shaft on the rotor side to a high rotational speed on the generator side.

The **brake** is installed in the drive train for emergency braking and for ensuring that the rotor is fixed, i.e. when performing maintenance on the turbine. To reduce the required torque from the brake, it is often placed on the high-speed shaft so that the gearbox transfers the torque to stop the rotating rotor.
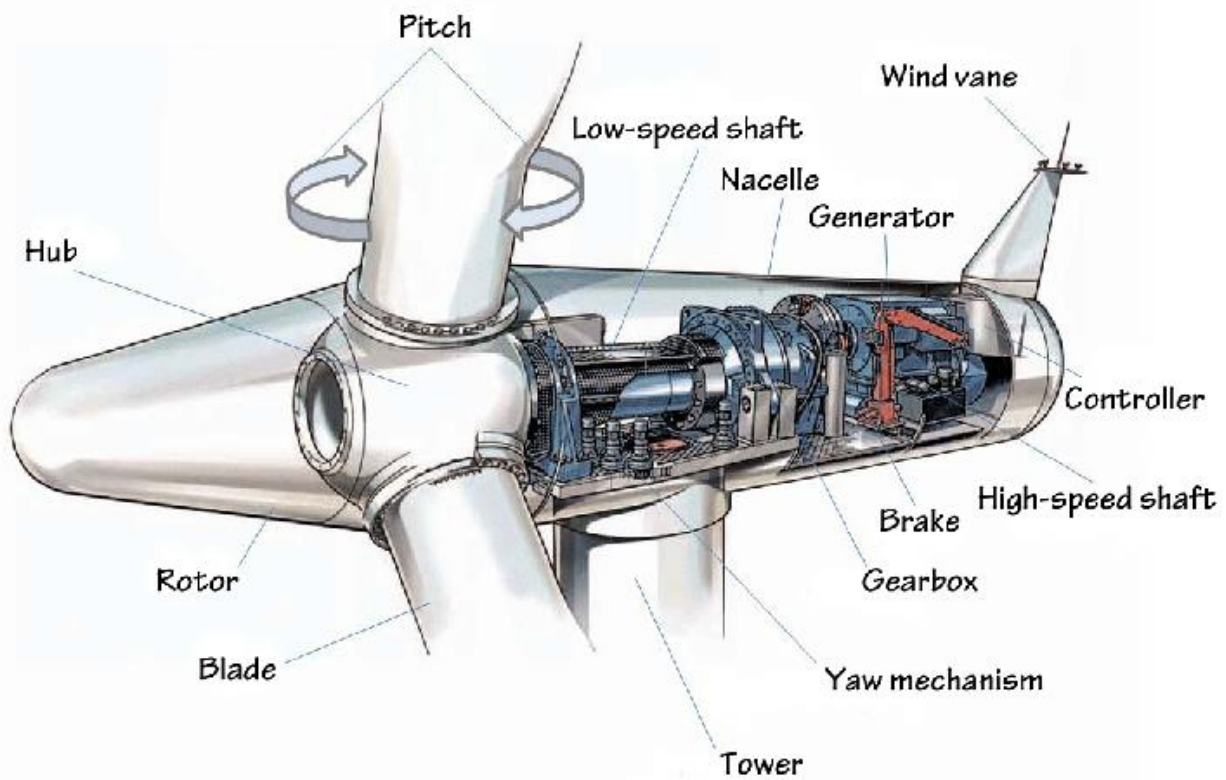


*Figure 3: Main parts of wind turbine*

The **nacelle and main frame** consist of housing, a bedplate and a yaw system, which allow the rotor to orient according to the wind. All the components of the drive train are mounted on the bedplate and covered by the nacelle housing for protection. The yaw system can either be free or active and provides rotation of the nacelle and rotor so that the shaft of the rotor is aligned parallel to the wind. Free yaw systems mean that the rotor and nacelle can self-align with the wind, while the active systems use sensors and motors to turn.

The **support structure** is the lower part of the structure and distributes the forces onto the ground. The support structure includes the tower, the substructure, and its foundation. The

tower extends from the substructure to the nacelle to enable the appropriate elevation of the rotor. Typical types of the tower are tapered tubular member, truss structure and concrete towers. Towers are usually 1-1.5 times higher than the rotor diameter, depending on the site. For offshore wind turbines, the tower height depends on the local sea conditions and the height of the support structure.

For **offshore applications**, there are several types of support structures. Some of them are fixed to the bottom, while others are floating.

| Bottom fixed | Floating |
|---|---|
| Mono-tower structure (Monopile) | Spar |
| Tripod structure | Semisubmersible |
| Jacket structure | Tension Leg Platform (TLP) |
| Gravity structure | |

*Table 1: Offshore wind turbine support structures*

## 1.3   Floating support structures

Floating support structures have not explored as much as the bottom-fixed, but are now investigated in pilot projects and have a strong potential for development. Examples of projects of floating support structures are the Hywind project, the Blue H FCU project, the Floatgen project and the WindFloat project. Wind-wave combination structures taking advantage of both wind and wave energy in the same offshore construction, resulting in an attractive solution.

### 1.3.1   Spar

Spar floaters are designed like spar buoys with a long and narrow geometry. They have a large draught so that the center of gravity is quite low to provide stability, making the structure ballast stabilized. The structure is usually kept in place by catenary mooring lines, which can be fixed to the ground by different anchoring solutions or piles. A sketch of a spar floater support structure for offshore wind turbines is shown in Figure 4. An example of a Spar support structure design is the Hywind Tampen, also shown in Figure 4.



*Figure 4: Main design concept of floating spar design wind energy platform (left), Hywind Tampen wind energy platform (right)*

### 1.3.2   Semisubmersible

Semisubmersible floaters generally consist of several vertical cylindrical columns which are connected structurally above and below the water surface. The structure below the surface provides the necessary buoyancy for the unit. Plates at the bottom of the columns, reduce the heave motions caused by the sea waves.

An example of a semisubmersible support structure design is the WindFloat concept. It has been tested from 2011 with a 2 MW turbine operating outside Portugal. After five years of deployment, the test turbine was taken back to shore for decommissioning. The design of the first test structure has three columns protruding the water, where the turbine is placed on top of one of the columns, with the tower as an extension on the column. Water ballast is used to obtain the proper levelling of the structure and plates on the lower, submerged part of the columns provide damping.



*Figure 5: Main design concept of semi-submersible floating design wind energy platform (left), WindFloat Atlantic wind energy platform (right)*

### 1.3.3   Tension Leg Platform

Tension leg platforms (TLPs) have positive buoyancy and are tied down to the bottom with cables loaded in tension. The cables can be fixed to the bottom using gravity-based foundations lying on the bottom, suction buckets or piles. Heave and pitch motions are very small for this floating concept, since the tension in the cables are effective in keeping the turbine in place for these degrees of freedom.



*Figure 6: Main design concept of Tension Leg Platform wind energy (left), HEXAFLOAT Tension Leg Platform (right)*

## 2 Renewable Energy Multi-Purpose Floating Offshore System (REFOS)

The Renewable Energy Multi-Purpose Floating Offshore System (REFOS) structure encompasses an array of hydrodynamically interacting OWC devices, moored through tensioned tethers as a TLP platform supporting a 10 MW wind turbine. The system consists of a triangular platform supported by cylindrical floaters with the WT mounted on a supporting central cylinder at deck's center and the cylindrical OWC devices at its corners. The OWC consists of two concentric cylinders, with the water entering through the subsurface opening into the annular chamber between the two cylinders that contains air. The wave action causes the captured water column to rise and fall like a piston, compressing and decompressing the air. As a result, there is an air flow moving back and forth through an air turbine coupled to an electric generator. In the center of the platform a cylindrical solid body is arranged to support the WT.



*Figure 7: Renewable Energy Multi-Purpose Floating Offshore System (REFOS) design*

### 2.1 Original structure description

#### 2.1.1 Floaters dimensions

The REFOS floating system has been developed for supporting a 10 MW reference wind turbine. It encompasses an array of three identical OWC devices, which can oscillate about their mean equilibrium position moving as a unit in a triangular configuration. In the center of the platform, a solid cylindrical body is placed to support the WT.

A summary of the geometric characteristics of the floater, including the diameters of each of the members and the mass distribution among the constitutional parts of the platform is provided in Table 2. These properties are all relative to the undisturbed position of the platform. The mass, including ballast, of the floating platform is 9550 t. This mass was calculated in a way that the

combined weight of the rotor-nacelle assembly, tower, platform, plus the applied TLP pretension and the weight of the mooring system in water, balances with the buoyancy (i.e., weight of the displaced fluid) of the platform in static equilibrium position in still water.

| Oscillating Water Column (OWC) Devices | |
|---|---|
| Diameter of inner concentric cylindrical body | 14.00 m |
| Draught of inner concentric cylindrical body | 20.00 m |
| **Central cylindrical body supporting WT** | |
| Diameter of main column | 12.00 m |
| Draught of main column | 20.00 m |
| Diameter of pontoons and cross braces | 1.600 m |
| **Mass of the Floater** | |
| Mass of each oscillating chamber | 1140 t |
| Mass of each concentric cylindrical body | 828 t |
| **Mooring system** | |
| Number of tendons | 3 |
| Depth to anchors below SWL (Water depth) | 180 m |
| Mooring line length | 160 m |

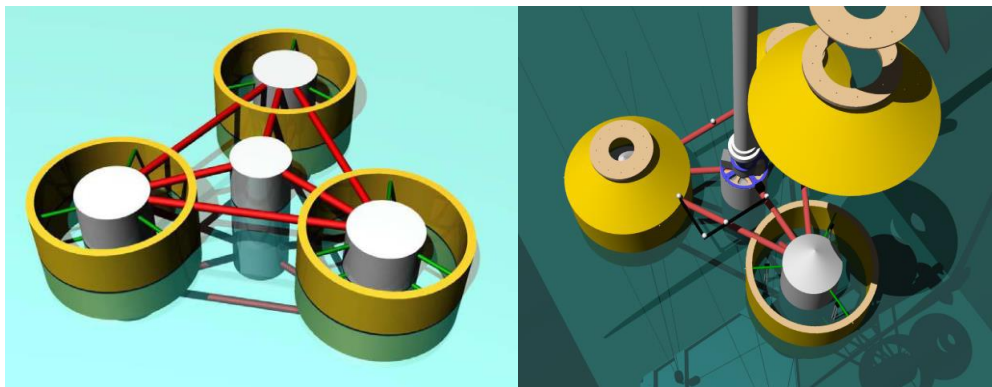Table 2: Main design specifications of REFOS



Figure 8: REFOS' main parts

The number of longitudinal and ring stiffeners, their spacing and the basic dimensions of the cross section of the stiffeners were determined. The three circumferential and the central column cylinders were reinforced using longitudinal and ring stiffeners of T-profile, as shown in Figure 9. Fifteen (15) longitudinal stiffeners at 2.16 m spacing were used for each circumferential column cylinder, while twenty (20) stiffeners at 1.57 m spacing were used for the central column cylinder. Moreover, thirty-four (34) ring stiffeners at 1.30 m spacing were used for the circumferential column cylinders and thirty-five (35) stiffeners with 1.07 m spacing were used for the central column cylinder.
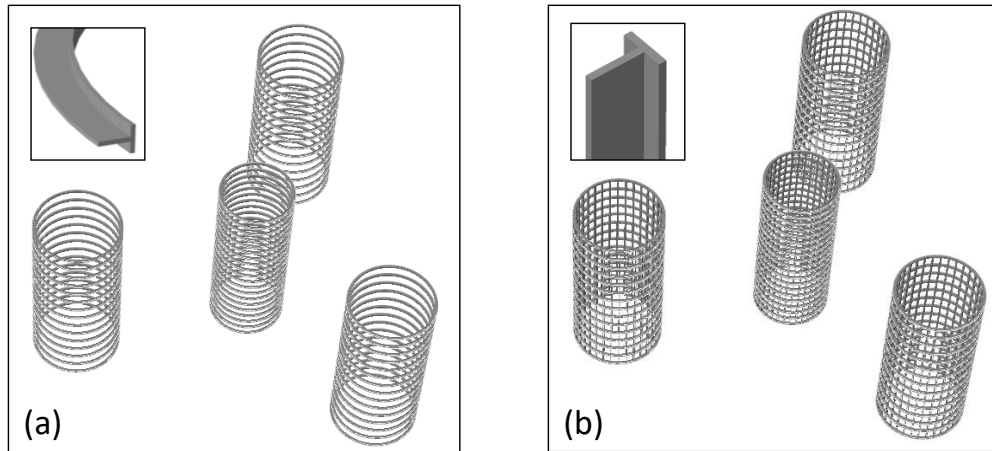
*Figure 9: Grid of stiffeners*

### 2.1.2 Mooring system

To secure the platform from changing position, the floating structure is moored with a TLP mooring system of three tendons spread symmetrically about the platform Z-axis. The fairleads (body-fixed locations where the mooring tendons attach the platform) are located at the base of the offset columns, at a depth of 20 m below SWL. The anchors (fixed to the inertia frame) are located at a water depth of 180 m below SWL. Each of the three tendons has an upstretched length of 160 m.

## 2.2 Preliminary results

Preliminary numerical simulations have demonstrated that the connection between the brace and the vertical cylinder, constitutes the critical structural detail of the floating system under consideration, as shown in Figure 10, significantly affecting the fatigue design of the floating platform. For that reason, extensive research has been conducted to further investigate the mechanical behavior of the joint under fatigue and the ultimate capacity of the joint.
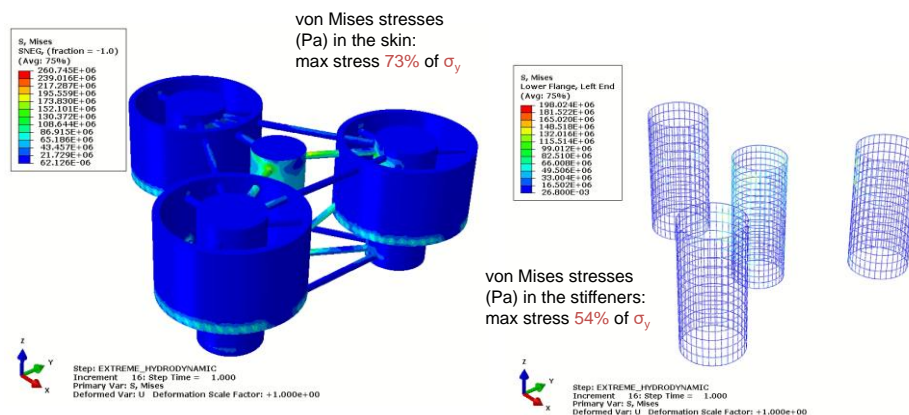


*Figure 10: Preliminary results of the floaters and braces*

## 2.3    Research targets

According to the preliminary results, extensive research has been necessary to derive more information about the mechanical behavior of the joint. As it will be explained later in section 3.3, no similar tubular joint has been analyzed before and for that reason no data were available about the fatigue and ultimate capacity of the joint. The special characteristics of the joint are described later in section 3.3.

For that reason, a detailed numerical model is developed, which includes the geometry of the weld between the skin and the brace. Target of the research was to investigate the mechanical behavior of the joint under fatigue and the ultimate capacity of the joint. For evaluating the numerical model, experimental results have been considered and compared with the numerical results.

## 2.4    Specimens' description

Specimens are approximately 1/6 scale physical models of the welded joints between the vertical buoyancy cylinders (pontoon) and the braces of a prototype floating structure. The two vertical tubular members of the joint, referred to as "primary or main brace" and "secondary brace", have a nominal cross-section 267 mm (diameter) × 8 mm (thickness), whereas the steel curved panel, called "shell", has 6 mm thickness and represents the main vertical cylinder, as shown in Figure 11. The brace-to-shell angle is 90 deg. In addition, a grid of longitudinal and transverse stiffeners has also been welded at the inner surface of the shell.



*Figure 11: REFOS Specimens main dimensions*

## 2.5    Experiments

### 2.5.1    Experiments' target

Physical experiments have been performed in the Laboratory of Reinforced Concrete Structures and Technology, Department of Civil Engineering, University of Thessaly. In those experiments,

both the ultimate capacity of the joint and the fatigue design life under different levels of constant-amplitude loading has been determined.

### 2.5.2    Experimental setup

The experimental setup arrangement is shown in Figure 12. The central main brace member of the specimen is connected to a 500-kN-force-capacity MTS hydraulic jack, installed in  horizontal position, using an appropriate hinge system (Figure 5a) and the "curved" shell is rigidly connected to the testing floor through HEA steel beams (Figure 5b). The horizontal load is applied at the top of the brace in the brace-to-shell plane (in-plane bending), at a distance of 595.7 mm from the meridional axis of the outer shell surface to the centerline of the bolted connection.
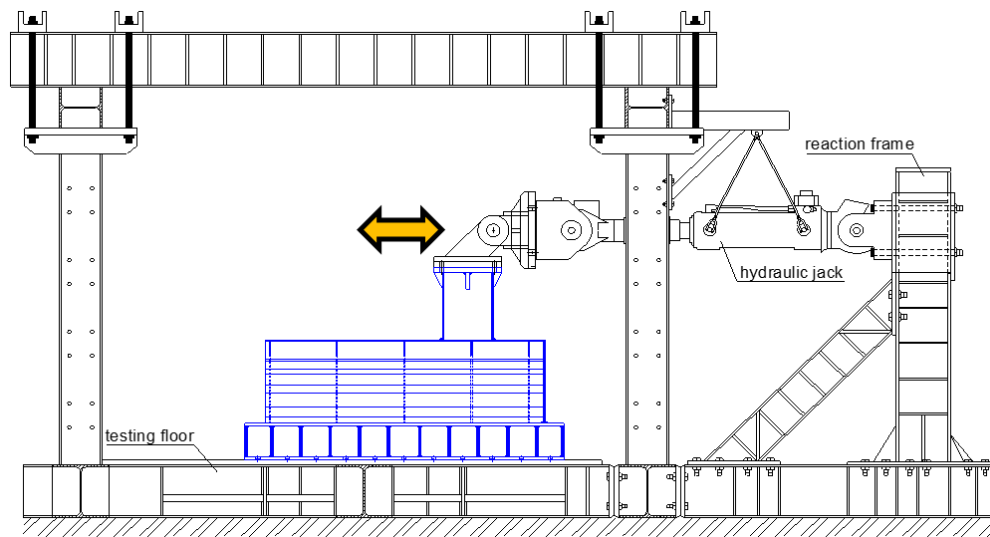


*Figure 12: Experimental setup*

### 2.5.3    Data allocation

The instrumentation consists of two wire-position transducers used to measure the load horizontal displacement at the end plate of the main brace (Figure 13) and a number of strain gages placed at the critical locations near the brace-to-shell welded connections (Figure 13).

The "crown" location of the central brace-to-shell connection was instrumented with strain gages and monitored throughout each fatigue and monotonic test. The strain measurements have been obtained using uniaxial five-gage-strips placed at the crown position of the joint, perpendicular to the weldment-toe. The position of the gauges was decided according to the preliminary numerical model. The distance between adjacent strain gages within the five-gage-strip is 3 mm, with the first gage being placed 5 mm away from the weldment-toe.

In all specimens, during fatigue testing, water was dropped at the welded connection area of the joint, on the shell surface, for detecting the possible through-thickness crack (water leakage through the shell thickness). Additionally, the central brace was internally pressurized with air at a relatively low pressure of 1.0 bar in the case of failure inside the tube (loss of pressure).

*Figure 13: Experimental instrumentation; wire gauge (left) and strain gauges (right)*

Moreover, a camera was placed under the curved shell skin for the "inside" inspection of the specimens during testing. Finally, for better visual inspection in detecting crack initiation and propagation, the Magnetic Particle Inspection (MPI), a non-destructive testing method, was also adopted.

### 2.5.4 Experiments list

In total 10 specimens were subjected in loading. Two different types post-welding processes are examined: (a) without High Frequency Mechanical Impact (HFMI) post-weld treatment and (b) with HFMI post-weld treatment.

Two specimens were subjected to monotonic loading and eight specimens were subjected to high-cycle fatigue under a constant load amplitude $\Delta P$. The occurrence of a through-thickness crack is the adopted criterion for fatigue failure, according to relevant international standards and recommendations. Four load ranges, $\Delta P = P_{max} - P_{min}$ have been considered equal to 22.5, 27, 45 and 90 kN with a fatigue load ratio $R = P_{min}/P_{max}$ equal to 0.10, at a frequency ranging from 0.6 to 1.8 Hz. An overview of the experimental program is presented in Table 3.

### 2.5.5 Overall experiments results

In all specimens, the through-thickness crack occurred at the crown position of the main brace-to-shell welded connection, as shown in Figure 14**Error! Reference source not found.**. It is interesting to notice that failure is very local in comparison with the size of the structure.

Fatigue crack initiation was observed both at the crown of the brace-to-shell weld-toe and along the weld of the central longitudinal stiffener at the inner side of the shell skin, underneath the crown position of the main brace, as shown in Figure 14. With further cycling, these cracks propagated mainly around the brace circumference and through the shell thickness, until a through-thickness crack occurred, indicated by the leakage of water or the loss of internal pressure. In specimens WTJ-3, WTJ-4 and WTJ-5 fatigue cracks started and propagate from outside of the brace while in specimen WTJ-6 from inside of the brace.

| Specimen | Load range $\Delta P = P_{max}-P_{min}$ | Nominal stress range (MPa) | Type of welding process |
|---|---|---|---|
| **WTJ-1** | monotonic loading | - | Manual with hammer peening |
| **WTJ-3** | 90 | 120 | |
| **WTJ-4** | 45 | 60 | |
| **WTJ-6** | 27 | 36 | |
| **WTJ-5** | 22.5 | 30 | |
| **WTJ-2** | monotonic loading | - | Manual without hammer peening |
| **WTJ-7** | 90 | 120 | |
| **WTJ-8** | 45 | 60 | |
| **WTJ-9** | 27 | 36 | |
| **WTJ-10** | 22.5 | 30 | |

Table 3: Overview of the experimental program



Figure 14: Crack at crown position (left), Crack at the "inner" skin side – stiffener (right)

# 3 Tubular joints design

Structural hollow sections, both circular (CHS) and rectangular (RHS), are widely used in numerous types of structural systems under different types of loading. In offshore platforms, tubular members are used because of their low hydrodynamic resistance, good structural and mechanical properties. Tubular members are connected to one an-other by special welded joints which are characterized by significant stress concentrations in the vicinity of the weldment. Under repeated loading, fatigue failures always initiate at the so called "hot-spot stress" areas, which are locations where the highest level of stress concentrations exist. The stress concentration depends on joint configuration, loading type and on local issues on the weld toe.

## 3.1 Types

The basic types of hollow section joints are presented below:
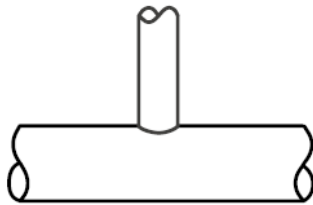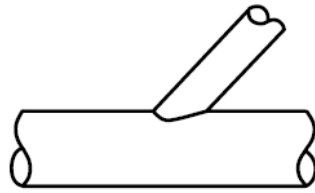


(a) CHS T-Joints      (b) CHS Y-Joints      (c) CHS X-joints
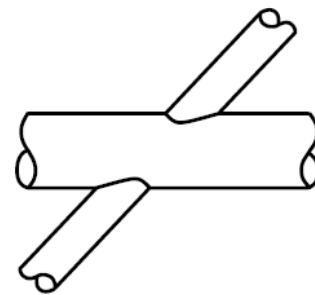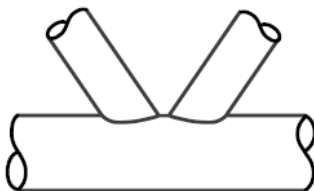
(d) CHS K-joints with gap

*Figure 15: Basic Tubular Joints Designs*

## 3.2 Hot Spot Stress and SCF

The hot spot stress (also called "geometric stress") method relates the fatigue life of a joint to the so-called hot spot stress at the joint, rather than the nominal stress. It takes the uneven stress distribution around the perimeter of the joint into account directly. The hot spot stress range includes the geometrical influences but excludes the local effects at the weld toe related to fabrication such as the configuration of the weldment (flat, convex, concave) and the local condition

of the weldment toe (radius of weld toe, undercut, etc.). The hot spot stress is the maximum geometric stress occurring in the joint where the cracks are usually initiated. In the case of welded joints, this generally occurs at the toe of the weldment.
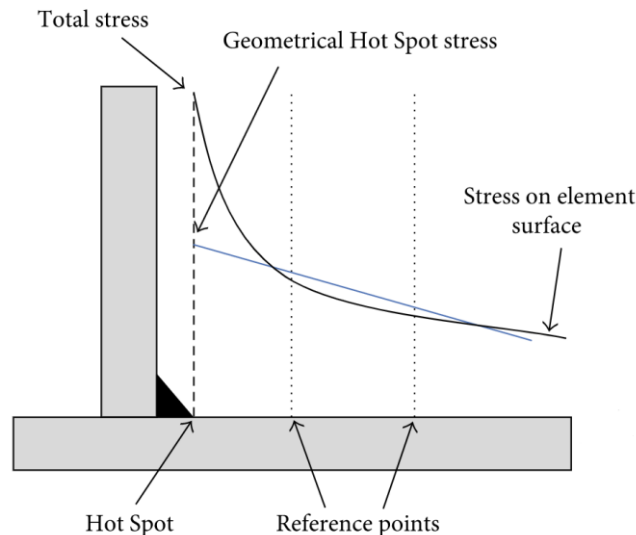


*Figure 16: Stresses distribution around welded joints*

The nominal stress can be described as the undisturbed far-field stress, or the stress calculated without taking into account the effect of geometric discontinuities such as weldment. In a bending case, the acting bending moment would be divided by the section modulus of the component in question.

The stress concentration factor (SCF) is the ratio between the hot spot stress of the joint and the nominal stress in the member due to a basic member load which causes this hot spot stress. The hot spot stress is determined at the weldment toe position from the stress field outside the region influenced by the local weldment toe geometry. The location from which the stresses have to be extrapolated, the so-called "extrapolation region", depends on the dimensions of the joint and on the position around the intersection.

For in plane bending the nominal stress is calculated by: $s_{r,ipb} = \frac{M_{ipb}}{W_{ipb}}$, where $W_{ipb}$ is the section modulus of the brace.

## 3.3   Available Stress Concentration Factors

Due to the wide use of the tubular joints for different applications, Stress Concentration Factors are calculated for different joint types and loadings. The values of SCF can be found in tables and charts according to the geometric parameters of the design.

These tables cover many of the tubular joints and load cases. For this case, the available data were not matching with the geometry of the available joints for two reasons. Data can be found for T-Joint with ratio of brace's diameter $d_1$ to chord's diameter $d_0$ greater that 0.2

$\left(\beta = \frac{d_1}{d_0} \geq 0.2\right)$. In this design, the ratio $\beta$ is equal to 0.12. The second reason is that underneath the skin, a frame of stiffeners is supporting and reinforcing the joint.

 For those reasons, a numerical model was developed and evaluated by experiments.

## 3.4  Calculation of Hot Spot Stress by Finite Element Analysis

As the weld toe is modeled as a sharp notch, the singularity effect may increase the stresses in the elements close to the weld. However, various types of stress extrapolation methods have been developed to overcome this problem.

Singularity refers to the location where stress value is unbounded in a finite element model. It is caused by a point or line load or moment, an isolated constraint point where the reaction force acts as a point load, or shape corner.

More reliable results are obtained by including the weldment in the finite element model. This makes mandatory the use of three-dimensional finite elements.

The SCF is calculated according to the DNVGL-RP-C203, 2016 edition, using the following equation.

$$SCF = \frac{Hot\ Spot\ Stress}{Nominal\ Stress}$$

The hot spot stress or geometric stress at tubular joints can be obtained by a linear extrapolation of the stresses calculated from analysis at positions at distances a and b from the weldment toe as indicated in Figure 17.

$$a = 0.2\sqrt{rt} \text{ and } b = 0.4\sqrt[4]{rtRT}$$
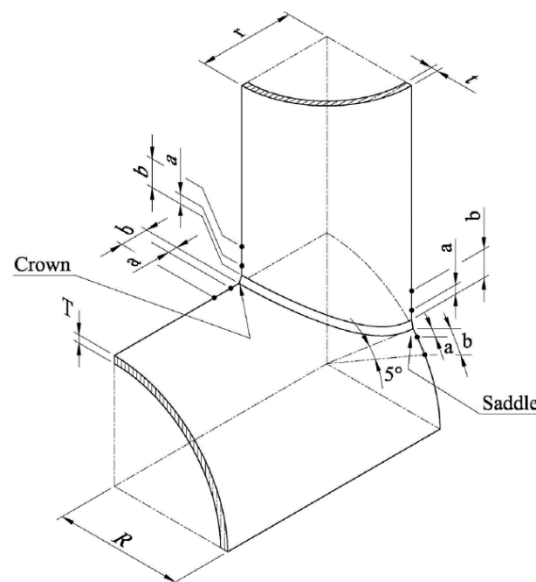


*Figure 17: Points of possible location of hot spot stress in tubular joints.*

# 4 Model description

In this chapter, the development of the initial design model is presented. The model was developed in the commercial Finite Elements Analysis software, Simulia, Abaqus. The chapter is de-scribes the steps needed to fully develop the model.

During the numerical model development, the total assembly is split in two regions. The region that is modelled using solid elements, and the region that is modelled using shell elements. The two regions can be seen below in Figure 18 with white and green color respectively. The reason for the present "hybrid model" approach in the model, is presented below in detail.
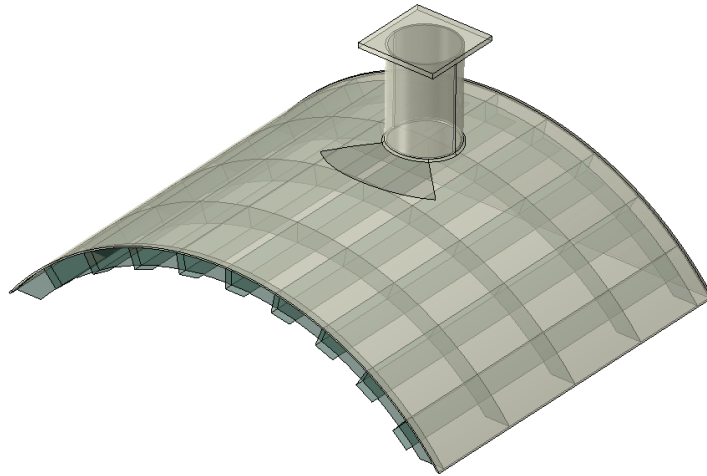


*Figure 18: Solid region (white), Shell region (green)*

## 4.1 Model Parts

The parts were designed either as solid bodies or surfaces. The dimensions of each part are shown below in Figure 19, based on the exact as-built drawings of the specimens tested in the laboratory.
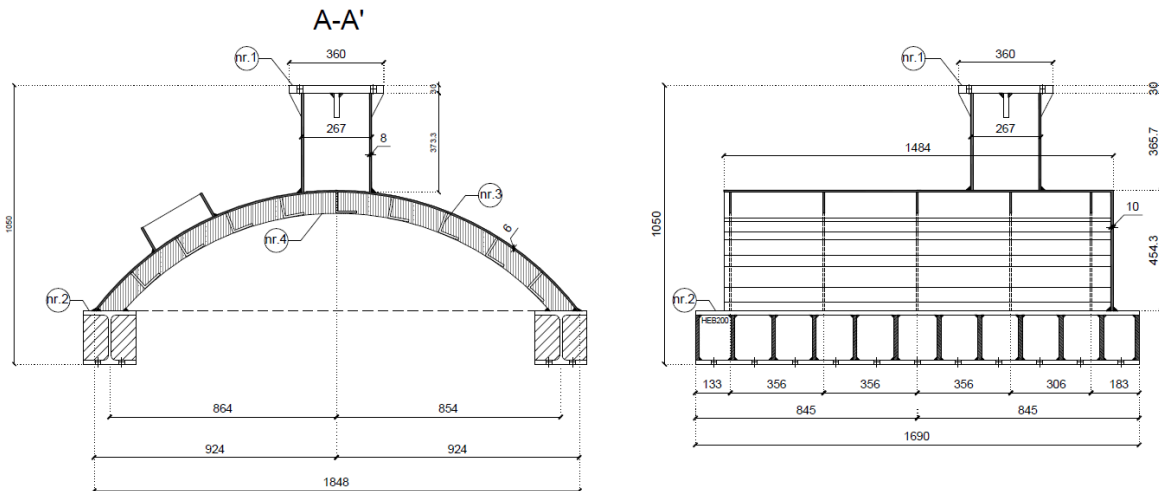


*Figure 19: Specimens dimensions*

The skin, the brace and the weldment were designed as one part to model the "integrated part" of the combined geometry, as shown in Figure 20, to avoid the use of any type of interaction between them. At the top of the brace a rectangular flat bar was added as in the experimental setup.
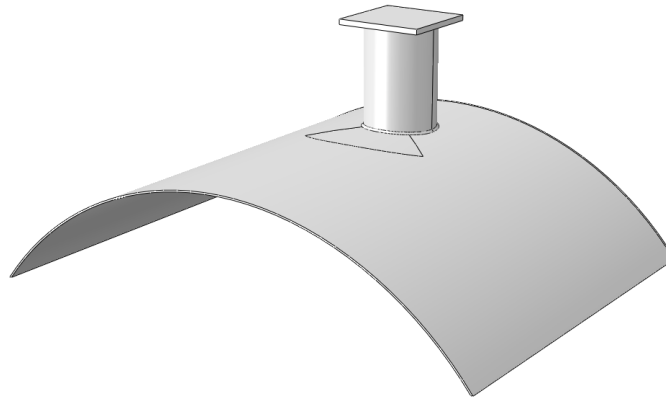


*Figure 20: Skin - Brace - Weldment part*

The back-plate, shown in Figure 21(a), was designed as a solid part individually. The horizontal and vertical stiffeners, as shown in Figure 21(b) and Figure 21(c) respectively, were designed individually, placed in as an assembly and the merged into one part. The reason for transforming the individual parts into one was to reduce the Number of tie connections used. In this way the model turned to be numerical easier.



**(a)**

**(b)**

**(c)**
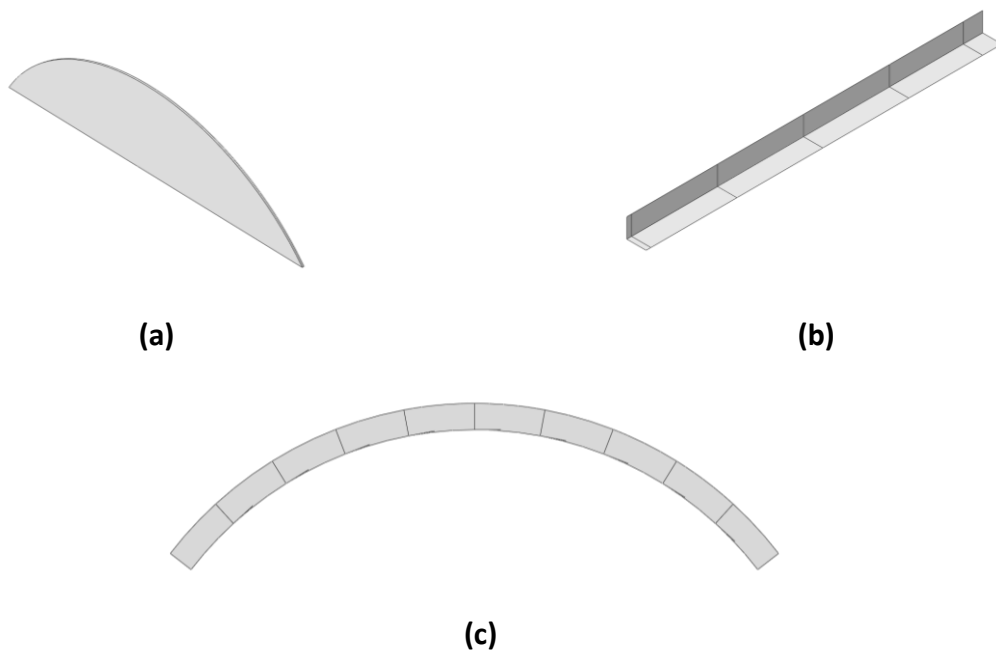
*Figure 21: (a)Back – plate, (b) Horizontal stiffeners, (c) Vertical stiffeners*

After completing the design, the three parts needed to be assigned material properties and connected each other. The three parts are presented in Figure 22.
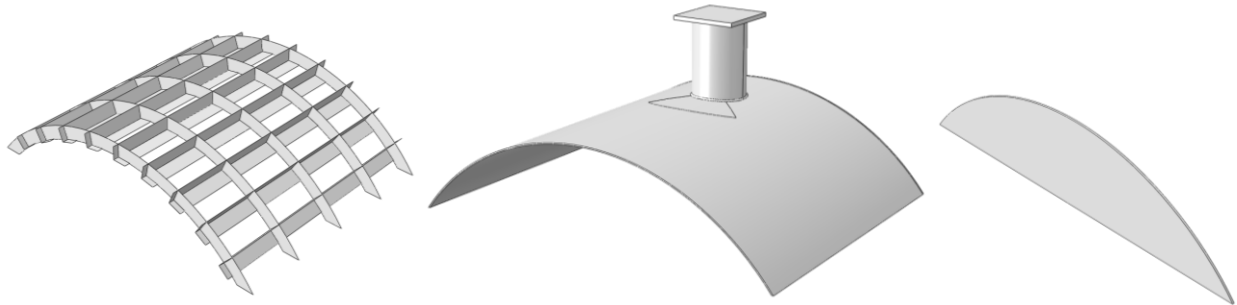


*Figure 22: Shell part (left). Solid parts (middle, right)*

## 4.2 Properties

The material used for the specimens is steel of grade S355. Tensile tests were performed for calculating the stress – strain curve. For importing the material properties in Abaqus, the engineering stress and strain values were converted to true stress and strain values, according to the following equations.

$$\sigma_{true} = \sigma_{engineering}(1 + \varepsilon_{engineering}), \varepsilon_{true} = \ln(1 + \varepsilon_{engineering})$$

The engineering and true stress-strain curves are shown below in Figure 23.
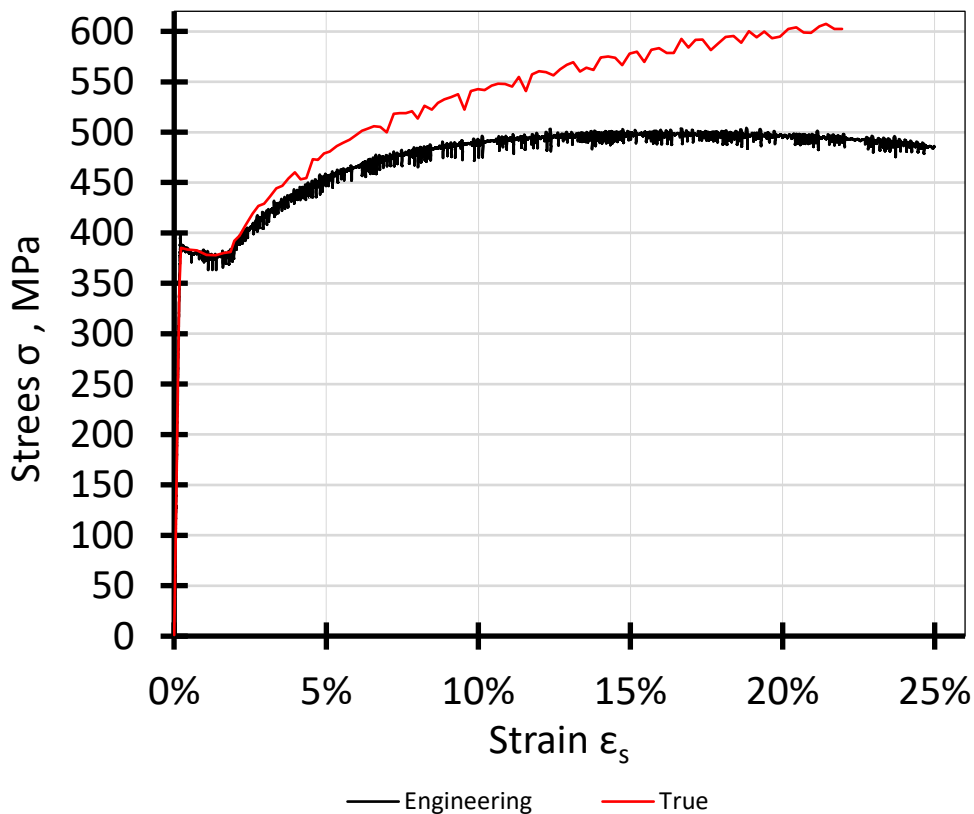


*Figure 23: Engineering and true stress - strain curves*

From the initial part of the stress – strain curve the Young's modulus was calculated at $E = 205\ GPa$ and after the 0.2% strain the plastic stress—strain curve was calculated and imported in Abaqus. The materials yield stress is $\sigma_y = 389\ MPa$ and its ultimate stress is $\sigma_{UTS} = 500\ MPa$. In addition, the curve was modified a bit for a smoother curve as shown below.
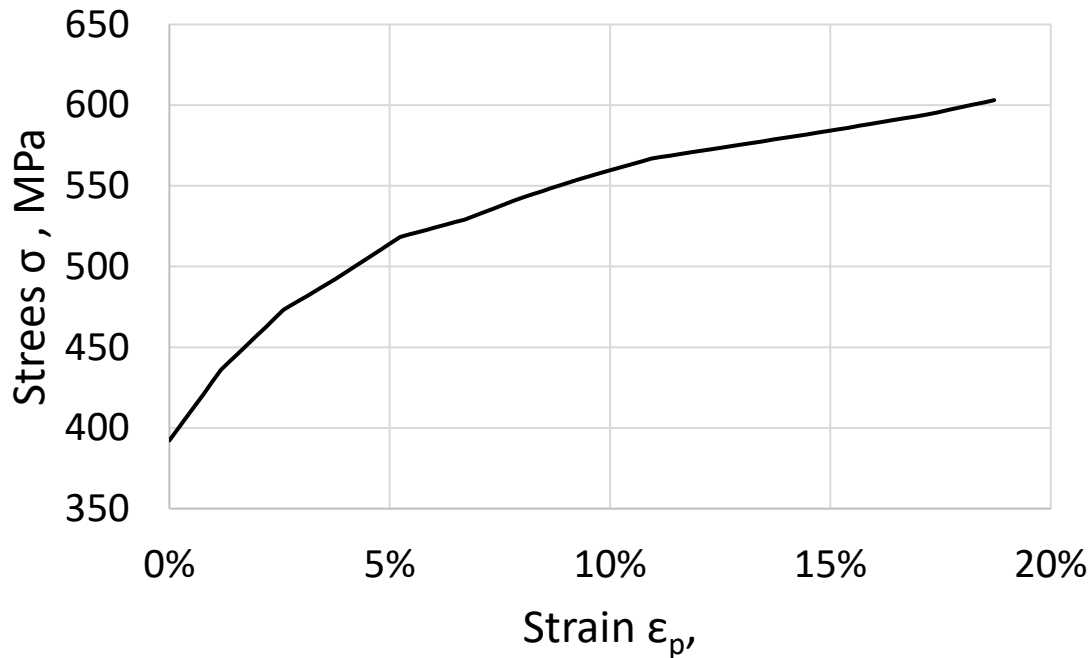


*Figure 24: Plastic region stress - strain curve*

The solid part was assigned with solid material properties and the shell parts was assigned with the shell material properties according to the thickness of each individual part.

## 4.3   Assembly

The three parts, mentioned at the end of Model Parts section, where combined in the assembly module. After placing the parts in the correct position, some useful partitions were assigned for easier meshing and post processing easier.

With the partitions the parts are divided into regions. A face partition was assigned on the skin for controlling the mesh density around the crown. In addition, a 400mm rigid bar was added, for modelling the free end of the hydraulic actuator in the experiment. The final assembly with the partitions is shown in Figure 25.
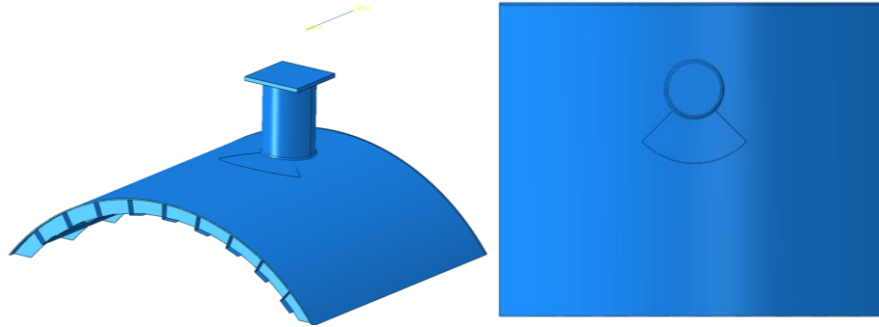
*Figure 25: Partitions in the final assembly*

## 4.4    Interactions

After placing the parts in the assembly module, the constraints are assigned. First, the grid of stiffeners is connected with the plate and the skin using the *"shell-to-solid coupling"* feature. The stiffeners are modeled using shell elements and the other two parts are modelled using solid elements. The plate is connected with the skin using the *"tie connection"* feature. The left point of the rigid bar (RF-1) is connected with the upper face of the plate using a *"kinematic coupling"* constraint. Coupling refers to all degrees of freedom besides the rotation about the x-axis (UR1). The final assembly with the constraints is shown in Figure 26.
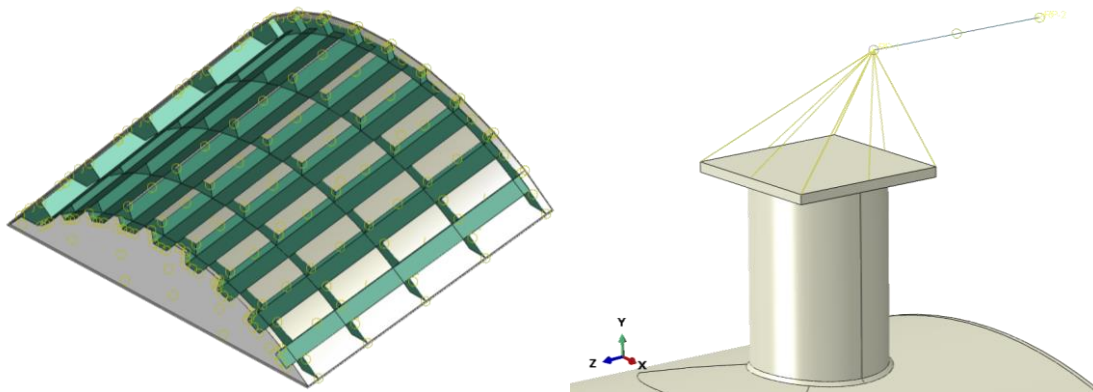


*Figure 26: Tie connection on the left with red markers, Coupling on the right with yellow lines*

## 4.5    Analysis procedure

The *"Static, General"* procedure is selected for the solution methods and time steps. For modelling the inelastic nonlinear geometry of the deformed joint in a proper manner, the NLGEOM property is activated. The number of time steps performed for the full analysis was decided to have an initial increment size 0.01 and maximum increment size 0.1.

## 4.6    Load

In the experimental setup, the lower side of the skin was fixed at all nodes (constraining all 6 degrees of freedom) and the load was applied on the right end of the rigid bar (RP-2). The same loading pattern is followed in the model. For the reference point two load cases are applied;

**(a)** a 10mm displacement and **(b)** a 45mm displacement in the direction of the negative z axis. The displacements on the x-axis (U1) and the y-axis (U2), as well as the rotations about y-axis (UR2) and z-axis (UR3) are constrained. During the experiments, the hydraulic actuator was fixed and expanding to the z-axis, and this is also simulated in the model. The free end of the actuator can rotate about x-axis. The final load pattern is shown in Figure 27.
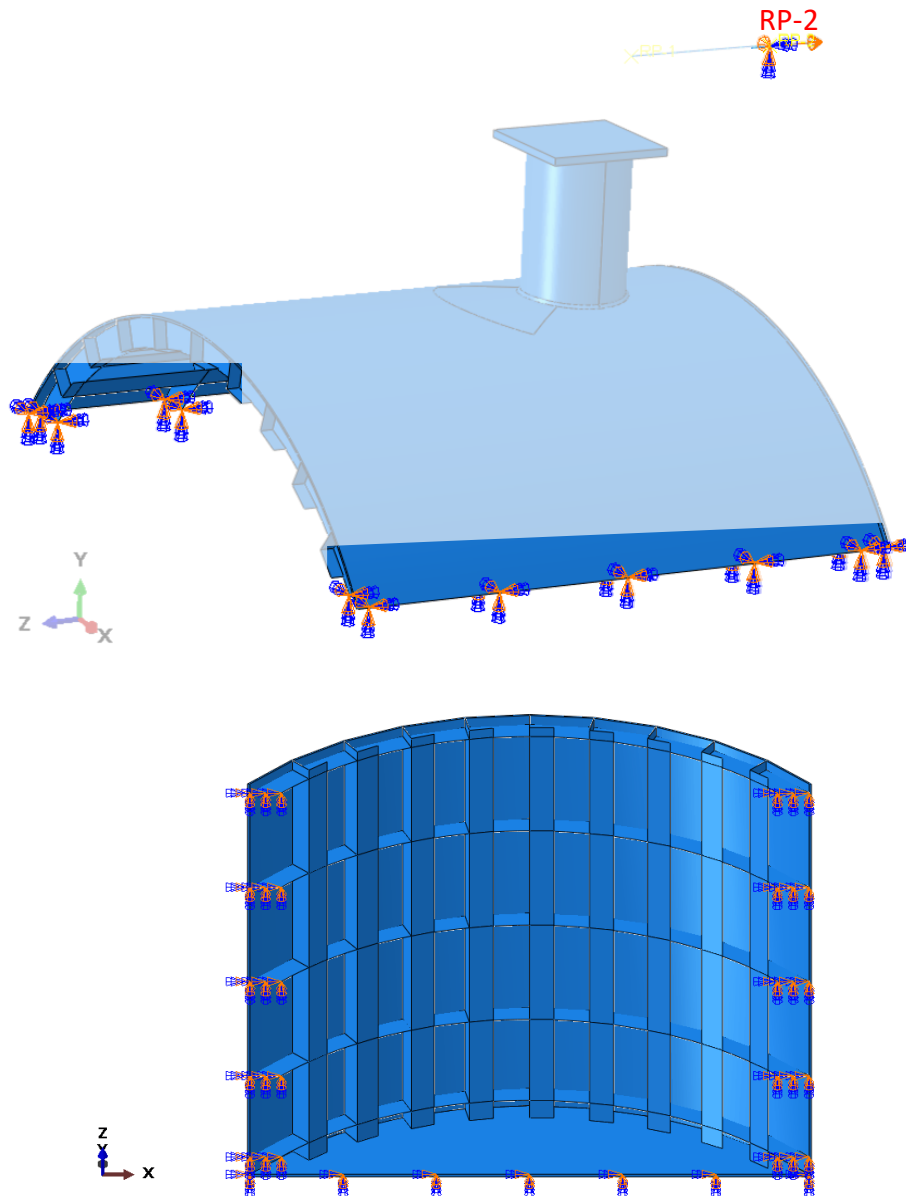


*Figure 27: Load pattern*

## 4.7    Finite element mesh

First, the model is split in partitions for easier and finer meshing in the critical regions. Three regions are given special attention in the model:

- Interface region between the skin and the brace's weldment
- Region around the brace of the skin (especially in the vicinity of the crown)
- Horizontal stiffener passing below the brace.

The generated mesh in each region together with a few comments reffering the meshing rules are shown below in Table 4.
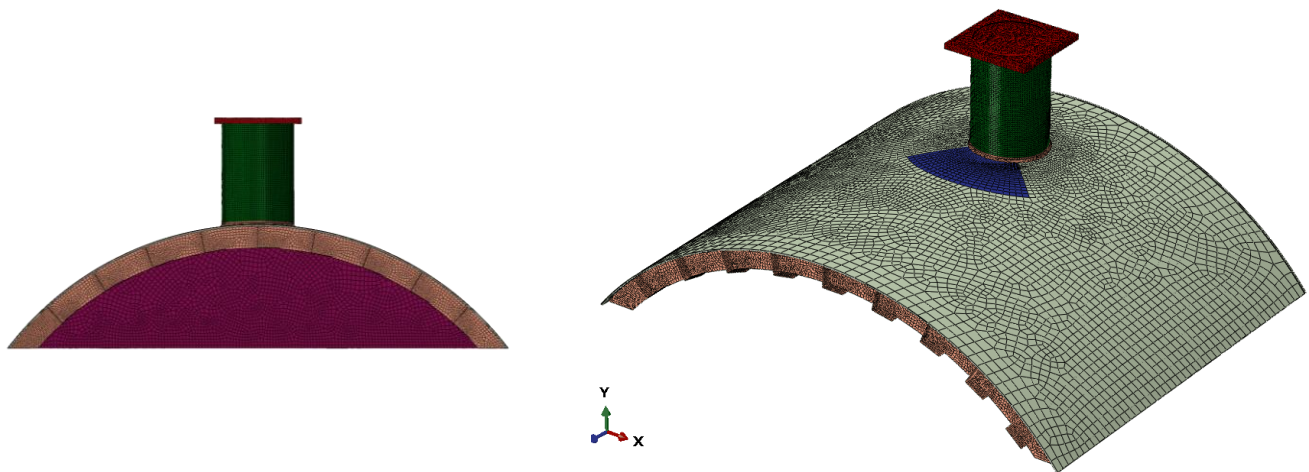


The model is meshed with 30mm x 30mm elements with special attention (mesh refinements) in the critical regions.
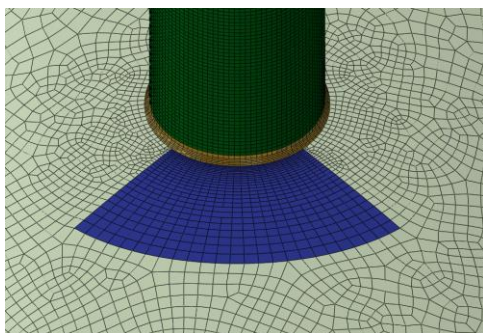


In the blue region, the element size is growing from 2mm to 8mm in the outer diameter, following the density of the strain gauges used in the experiment.
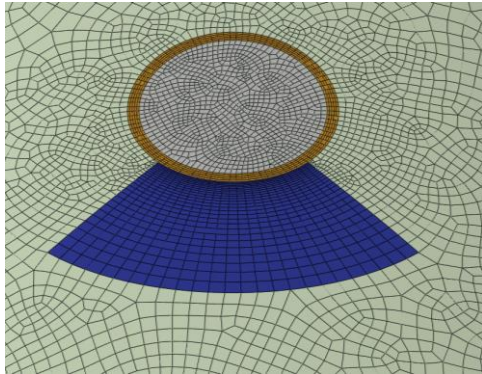
Around the weldment (golden region), 100 nodes are used for mesh refinement.
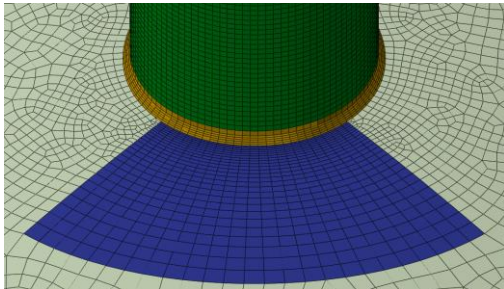


The weldment region (gold region) was meshed with 5 elements on weldment's face and leg.
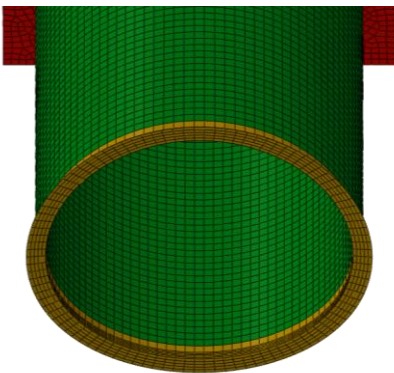


In the interface region (gold region) 5 elements through the thickness of weldments leg with the minimum distortion angle. The region is split in several sections and sweep mesh has been generated.
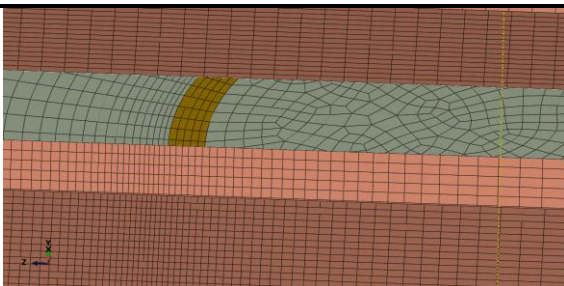


The stiffener below the brace (pink region) was refined close to the weldment's leg (gold region).

*Table 4: Meshing rules*

To decide the element type, multiple simulations have been conducted using reduced integration and fully integration, linear and quadratic elements. The details of the different cases are presented below in Table 5.

| Case name | Element order | Integration |
|-----------|---------------|-------------|
| LINEAR / REDUCED INT. | LINEAR | REDUCED |
| QUADRATIC / REDUCED INT. | QUADRATIC | REDUCED |
| LINEAR / FULL INT. | LINEAR | FULL |

*Table 5: Cases description*

The Reaction Force – Displacement of the Reference Point 2 (RP-2) for three different cases are shown below on Figure 28.

The curve of Case LINEAR / FULL INT. overestimates by a small amount the Reaction Force for the load case #1 (10mm) compared with the experimental curve. The error is less than 10% and the overall comparison is quite close to the experimental. For load case #2 (45mm) the Reaction Force is of this case is closer to the experimental and predicted a higher Ultimate Capacity of the Joint. The error is again below 10%. For those reasons it was decided to use the LINEAR / FULL INT. model.

The present model with the element type and meshing rules under consideration, consists of 59070 linear quadrilateral elements S4, 410 linear triangular elements S3 and 82909 linear hexahedral elements C3D8.
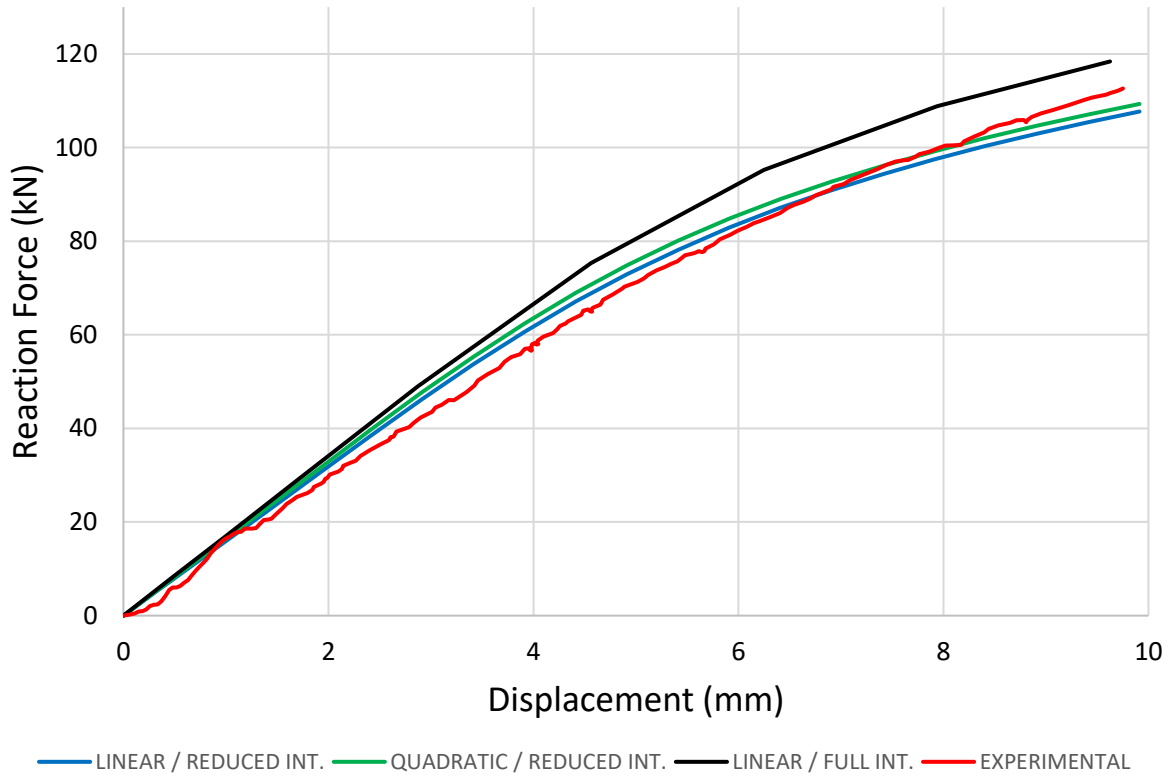
*Figure 28: Reaction Force - Displacement for different cases up to 10mm displacement (Load case #1)*
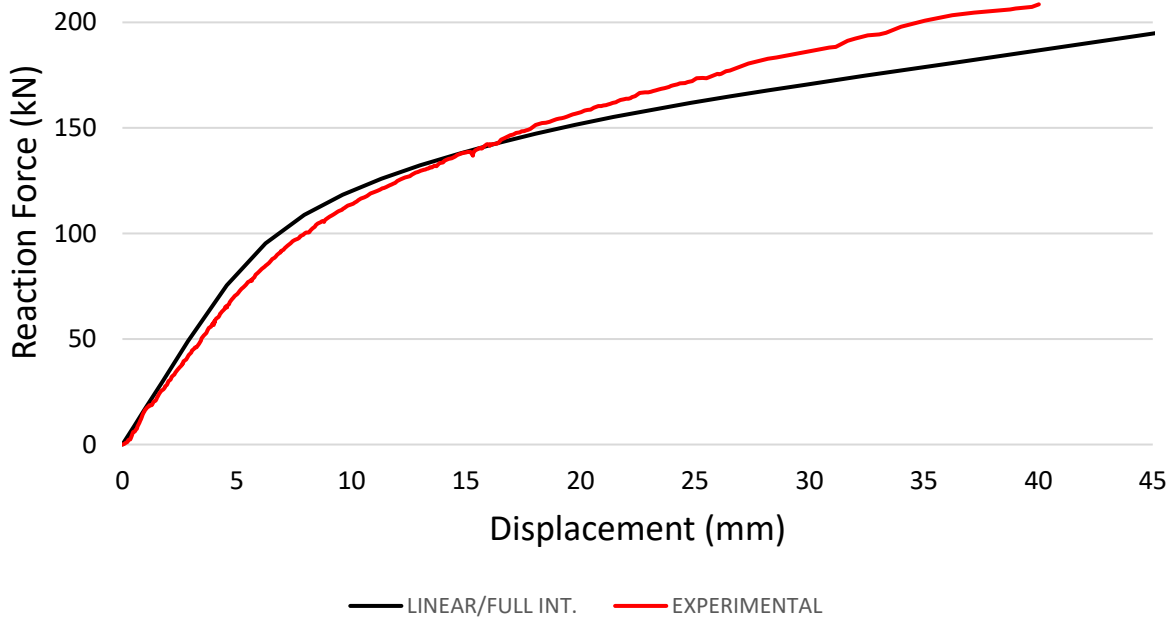


*Figure 29: Reaction Force - Displacement for different cases up to 45mm displacement (Load case #2)*

# 5   Numerical results

For validating the finite element model two issues had been considered, the experimental Reaction Force – Displacement diagram and some key observations during the experiments, on the crack initiation and propagation. The final targets of the research is to; **(a)** calculate a Stress Concertation Factor chart near to the weldment's crown (using Load Case #1 – 10mm), **(b)** calculate the resistance load up to 45mm and **(c)** identify the critical regions for crack initiation. In the next chapter, based on those results, two alternative preliminary designs will be provided, which improve the structural performance of the joint.

## 5.1   Critical regions

As mentioned in the previous section, there exist several critical regions that require attention. The analysis focuses on two regions: **(a)** the upper side of the skin at the weldment's crown and **(b)** the stiffener below the weldment's crown. The two regions are shown in Figure 30, both in the numerical model and the specimen.

Attention is also given in the "front" (Positive) side and the "back" (Negative) side of the central stiffener. The front side is shown with the green and the negative with the red on Figure 31.
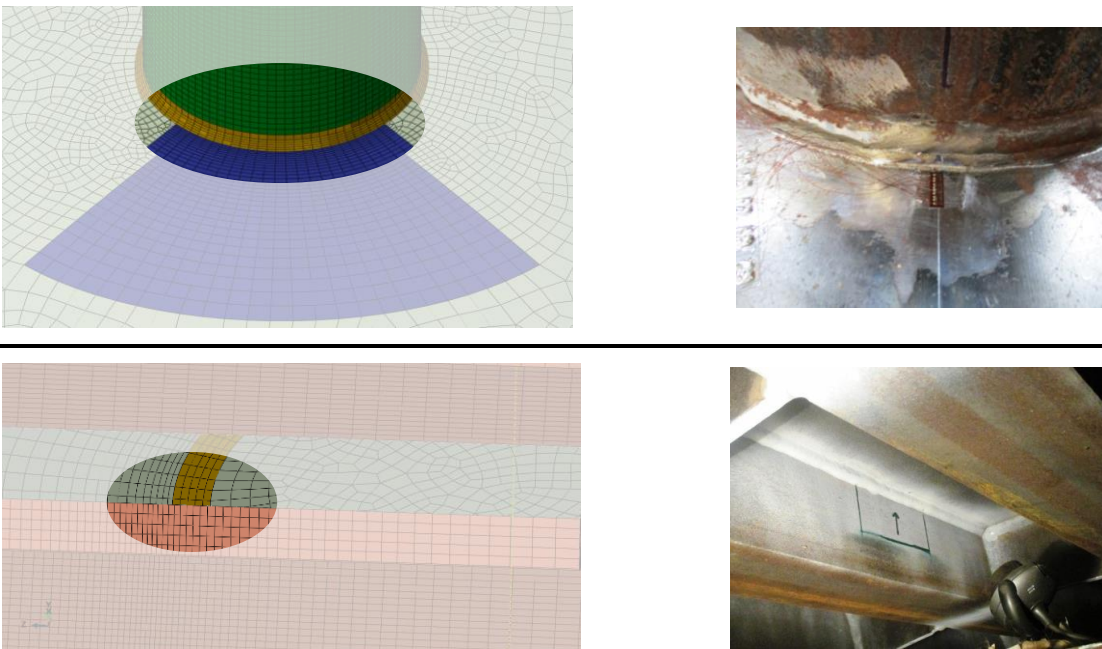


*Figure 30: Critical regions in the numerical model - specimen*
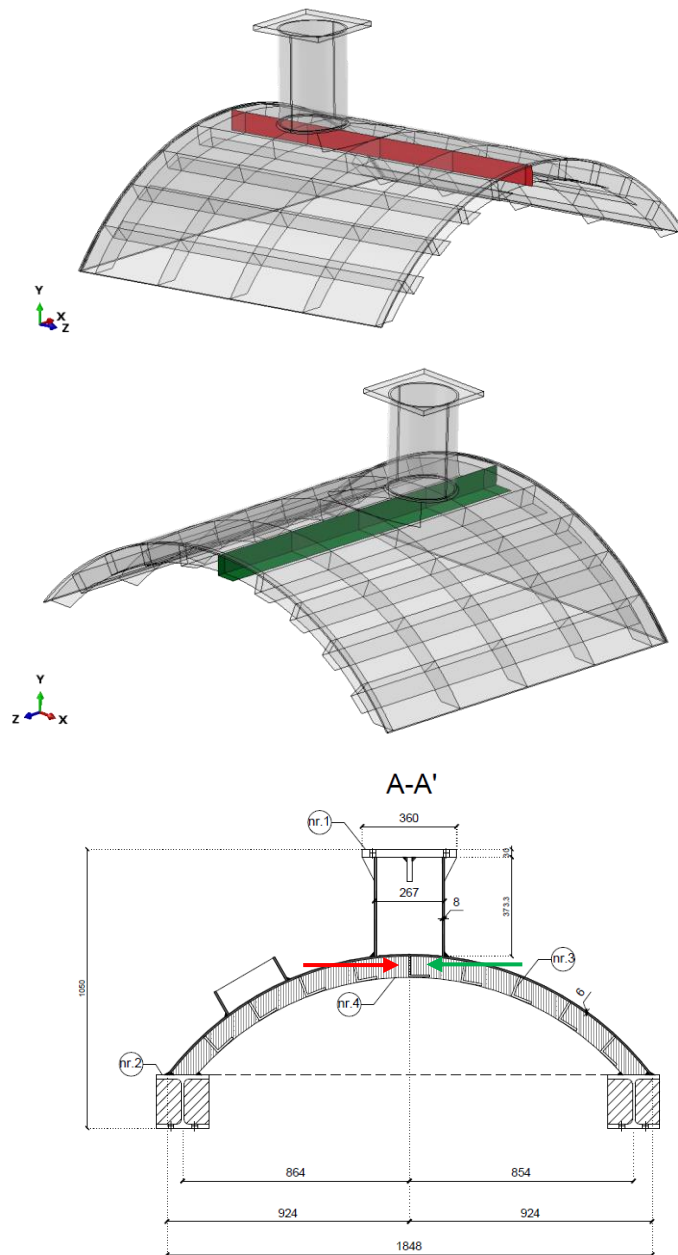
*Figure 31: "Front" and "back" side of the central stiffener*

## 5.2 Reaction Force – Displacement

In Figure 32 the Reaction Force – Displacement diagram obtained from the numerical model and the experimental curve are shown. The numerical model curve fits fairly well with the experimental curve, with an error below 10% both in the elastic and the plastic part.
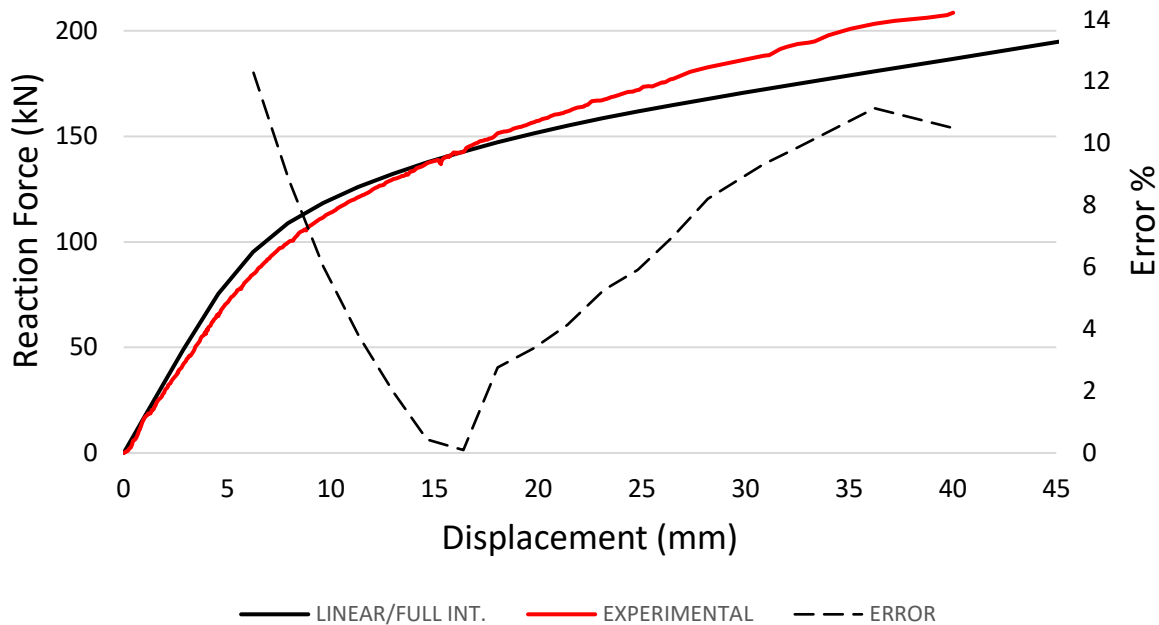


*Figure 32: Reaction Force – Displacement curve*

## 5.3 Crack initiation

In all specimens, during fatigue testing, water was dropped at the welded connection area of the joint, on the shell surface, for detecting the formation of through-thickness crack (water leakage through the skin shell). Additionally, the central brace is internally pressurized with air at relatively low pressure of 1.0 bar for detecting failure inside the tube (loss of pressure). Moreover, a camera was placed under the curved shell skin, for "inside" inspection of the specimens during testing. Finally for detecting crack initiation and propagation, the Magnetic Particle Inspection (MPI), a non-destructive testing method, has also been adopted.

The specimens where subjected to three different load amplitudes range ($\Delta P$ = 22.5kN, $\Delta P$ = 27kN, $\Delta P$ = 45kN and $\Delta P$ = 90kN). Based on the experiments the present analysis focuses on three load ranges: at $\Delta P$ = 27kN, $\Delta P$ = 45kN and $\Delta P$ = 90kN. The two critical regions for the ranges are compared in the following tables.

In the numerical model images, the stresses perpendicular to the crown, brace and the stiffener-skin connection are shown.

5.3.1    ΔP = 27kN

**SKIN TOP SIDE**



**through-thickness crack detail**
(660,017 cy)
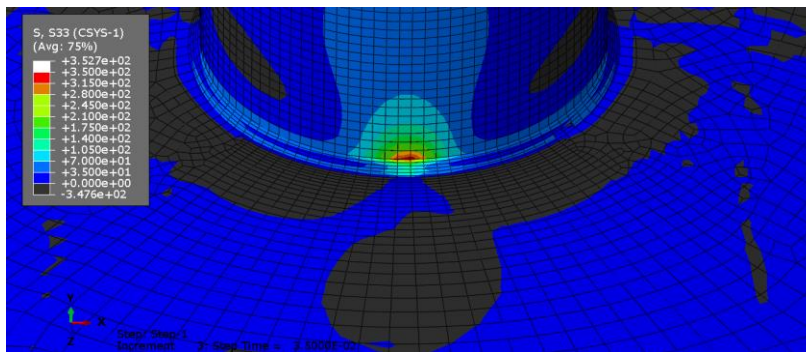


Distribution of stress perpendicular to the weldment on the **brace**
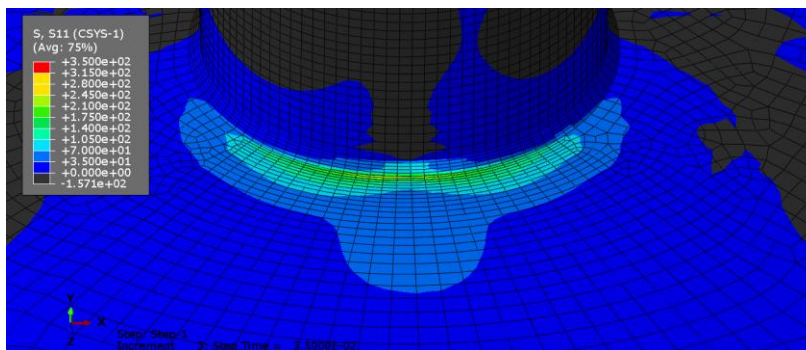


Distribution of stress perpendicular to the weldment on the **skin**
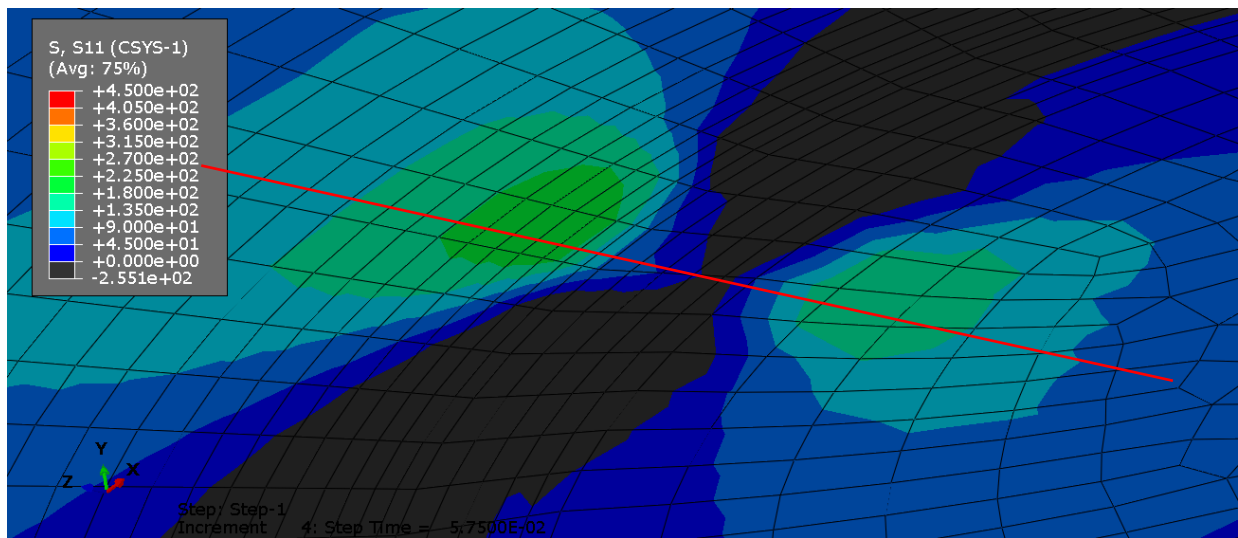
*Figure 33: Skin top side for ΔP=27kN*

In Figure 33 and Figure 34, for the ΔP = 27kN the stresses on the stiffener side is much higher compared with the top side of the skin. During the experiments, the crack initiated at the stiffener's side at about 600,000 cycles. Prior to this stage no crack was observed on the top side of the skin. Therefore, it can be concluded that for low range load, below 45kN, the stiffener side is critical, and the crack initiates at the stiffener – skin connection, below the skin and propagates through the skin.
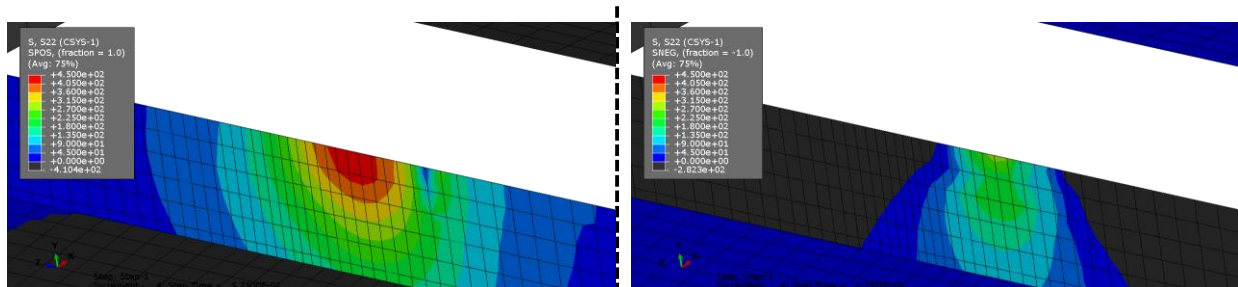
## STIFFENER SIDE /SKIN BOTTOM SIDE
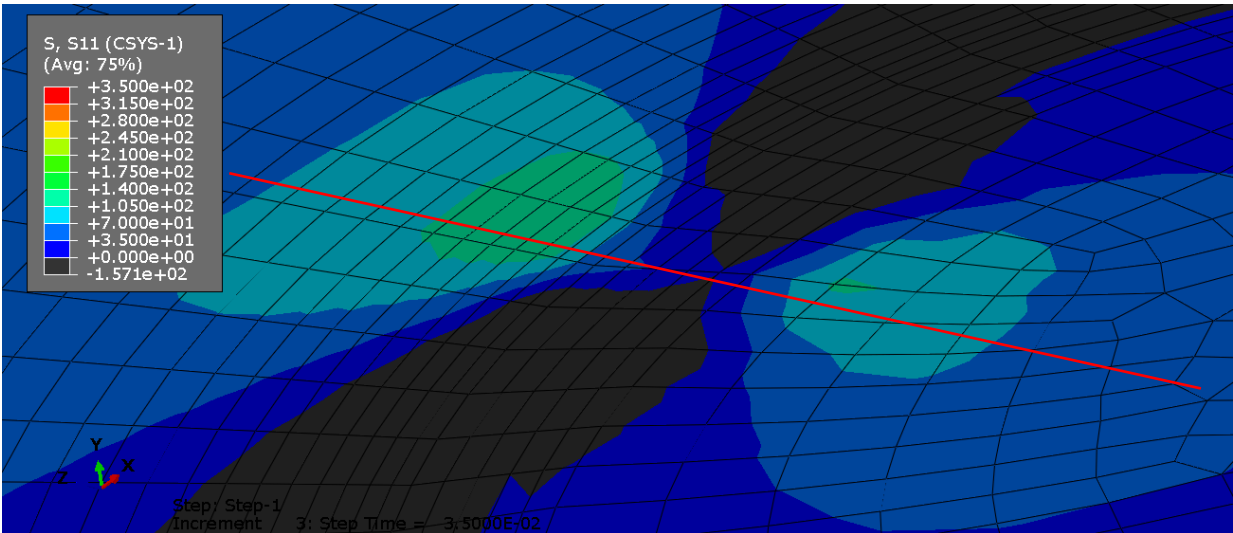


**through-thickness crack detail**
(660,017 cy)



Stresse at the bottom "inner" side of the skin – The red line shows the intersection of the stiffener with the skin.
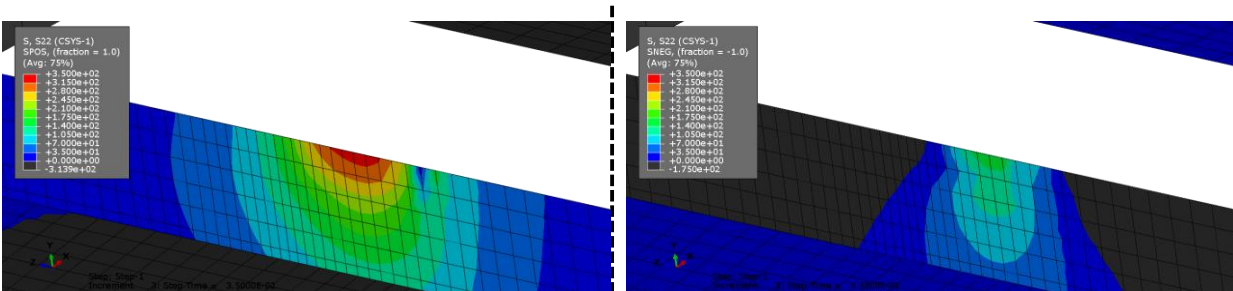


| Front side of stiffener (POSITIVE) | Back side of stiffener (NEGATIVE) |

*Figure 34: Skin bottom side for ΔP=27kN*

The distribution of stress perpendicular to the stiffener – skin weldment and on the inner skin side is presented in Figure 34. The stresses on the "front" side of the stiffener are higher compared to those at the "back" side. The same conclusion can be confirmed by the experiments, as no crack has been detected on the "back" side.

5.3.2   ΔP = 45kN

**SKIN TOP SIDE**



**no visible cracking**
(≈ 70,000 cy)
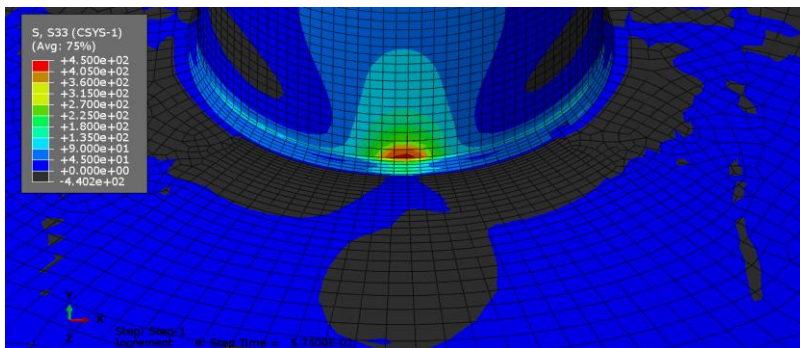


Distribution of stress perpendicular to the weldment on the **brace**
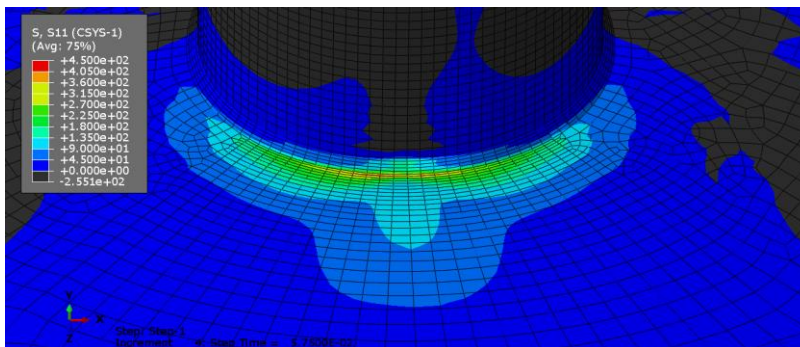


Distribution of stress perpendicular to the weldment on the **skin**

*Figure 35: Skin top side for ΔP=45kN*

The specimen with ΔP = 45kN was expected to undergo a more intense stress distribution in both regions, as shown in Figure 35and Figure 36. Again, stresses normal to the stiffener are higher compared to the upper skin side. In the experiments, prior to 70,000 cycles, no crack was observed at the crown. Instead, a crack initiated from the stiffener side at about 70,000 cycles.

## STIFFENER SIDE /SKIN BOTTOM SIDE



**through-thickness crack detail**
(88,329 cy)



Stresse at the bottom "inner" side of the skin – The red line shows the intersection of the
stiffener with  the skin.



Front side of the stiffener (POSITIVE) | Back side of the stiffener (NEGATIVE)

*Figure 36: Skin bottom side for ΔP=45kN*

5.3.3   ΔP = 90kN

## SKIN TOP SIDE



**first crack detection**
(≈ 3,000 cy)
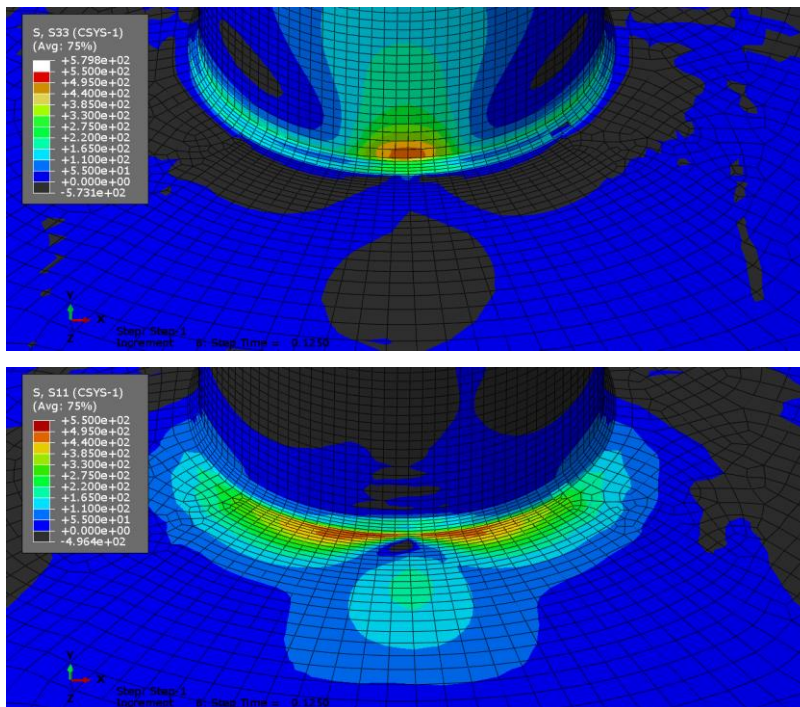


Field stress perpendicular
to the weldment on the
**brace**



Field stress perpendicular
to the weldment on the
**skin**

*Figure 37: Skin top side for ΔP=90kN*

For the specimen subjected to ΔP = 90kN, the stresses distribution is even higher compared to the two previous cases. As a result, the number of cycles leading to crack initiation are much lower. Here, a crack initiated from the skin side and stiffener side at the same time and led to a through thickness crack. In addition, at this range, high stresses are observed on the brace.

## STIFFENER SIDE /SKIN BOTTOM SIDE



**first crack detection**
(≈ 3,000 cy)
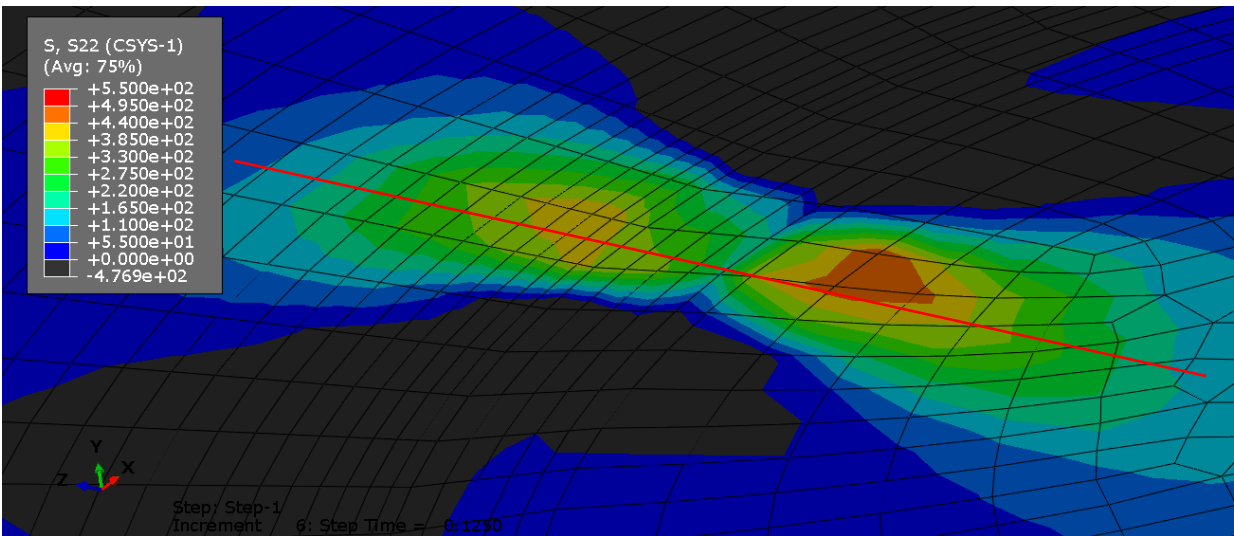


Stresse at the bottom "inner" side of the skin – The red line shows the intersection of the stiffener with the skin.



| Front side of the stiffener (POSITIVE) | Back side of the stiffener (NEGATIVE) |
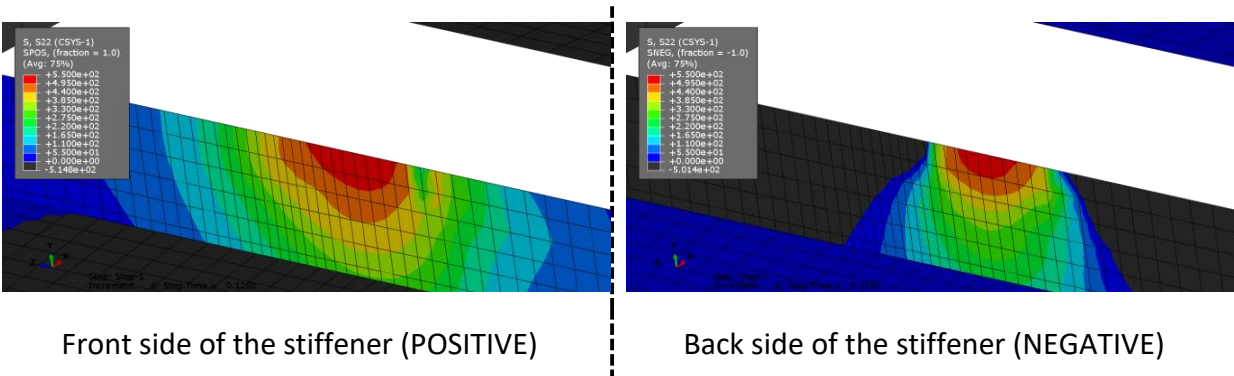
*Figure 38: Skin bottom side for ΔP=90kN*

### 5.3.4   Conclusion

From the previous observations, it is concluded that special attention should be given at the connection between the stiffener and the skin. According to this observation in the last chapter of this document, some alternative design will be presented, which may reduce the stresses on the stiffener side.

Another important observation is that the stresses on the left and right side of the crown are larger compared to the central part. This can be explained by the existence of the stiffener below the crown, which increases the resistance.

## 5.4   Overall model observation

Two of the specimens were applied a monotonic load till total failure. On the left and right side of the central stiffener the skin is raised much more compared to the central part. As shown in Figure 39, this can be observed both in the experiments and the numerical model. This can be explained by the existence of the central part, which reduces the stresses as well, as mentioned in the previous paragraph.
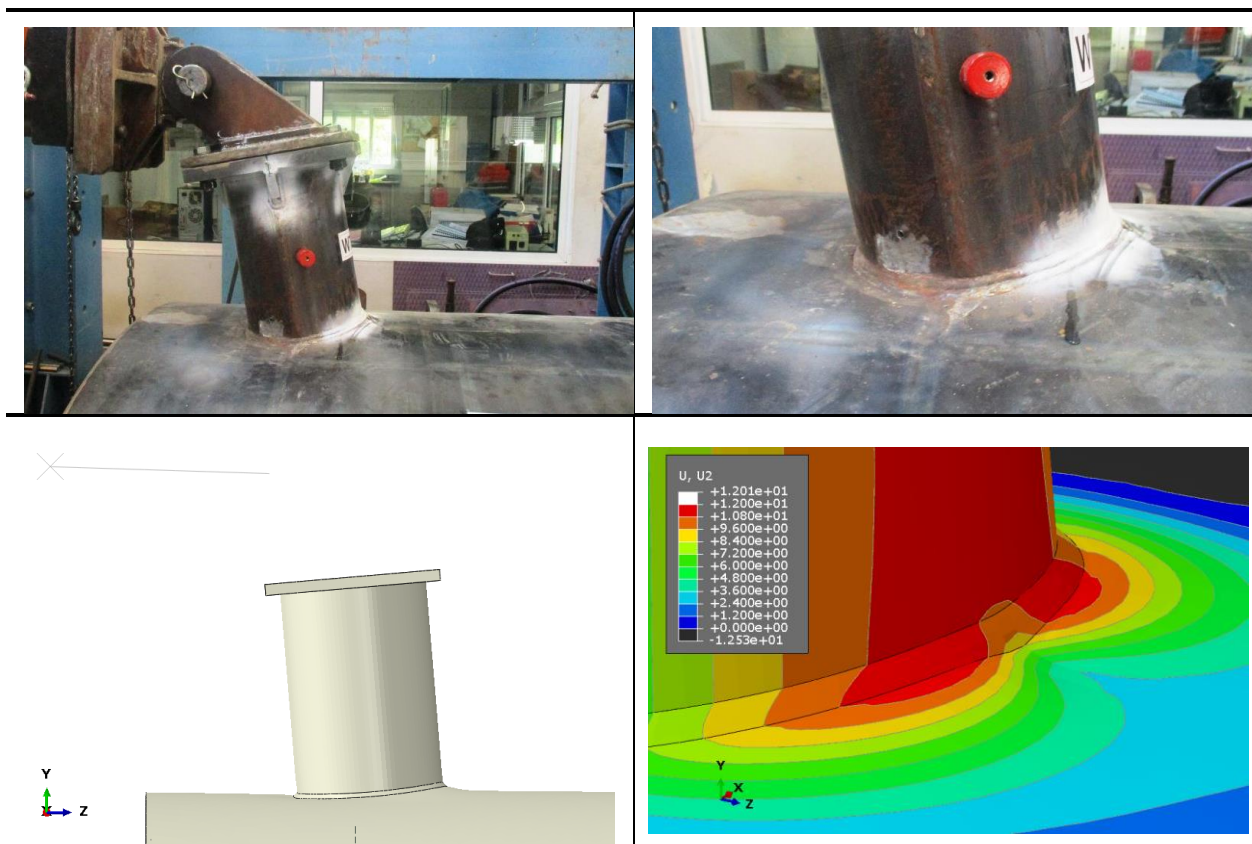


*Figure 39: Overall specimen deformation comparison*

## 5.5   Stress Concentration Factor (SCF) chart

A target of the research was to calculate the value of Stress Concentration Factor around the brace as there are no available data on the literature for such a welded joint.

The SCF chart was calculated according to the DNVGL-RP-C203, 2016 edition. The SCF is calculated using the following equation.

$$SCF = \frac{Hot\ Spot\ Stress}{Nominal\ Stress}$$

The Hot Spot Stress is calculated using two points for extrapolation. The two points are at distance a and b from the crown.

$$a = 0.2\sqrt{rt} \text{ and } b = 0.4\sqrt[4]{rtRT}$$

The final SCF chart is shown on Figure 40.
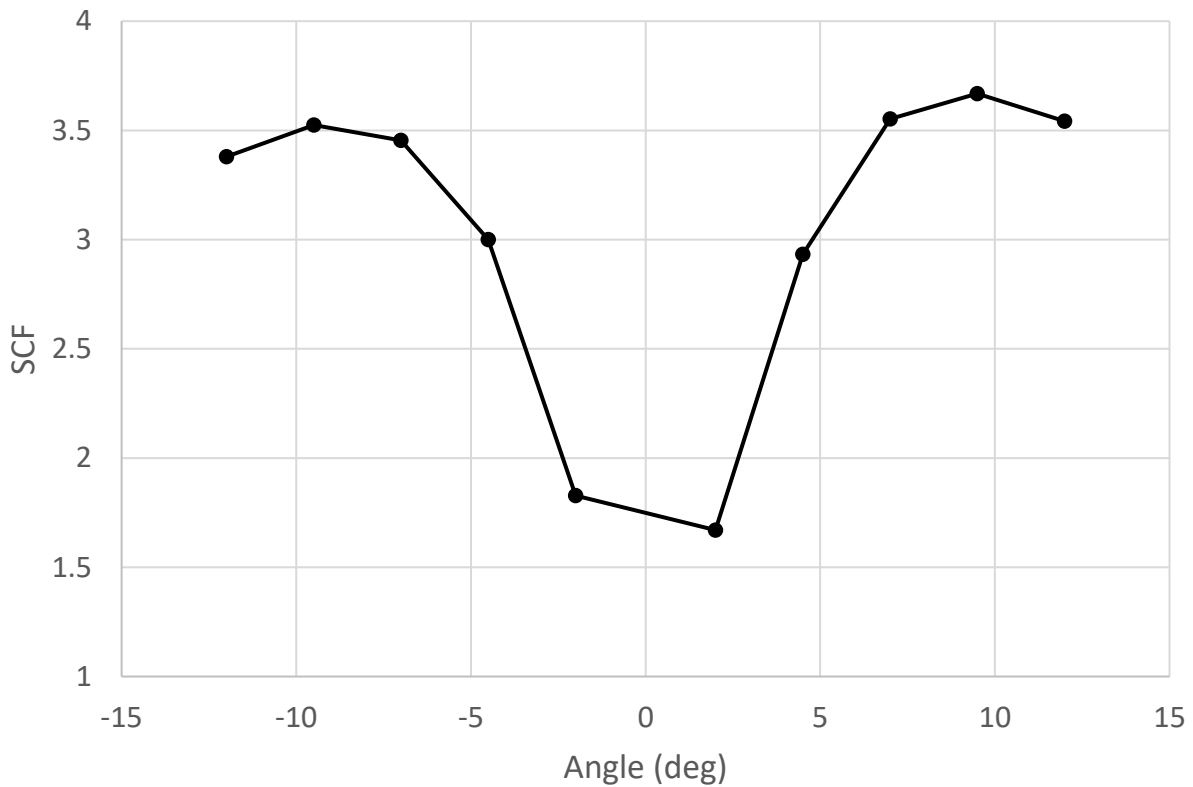


*Figure 40: Stress Concertation Factor chart around the brace*
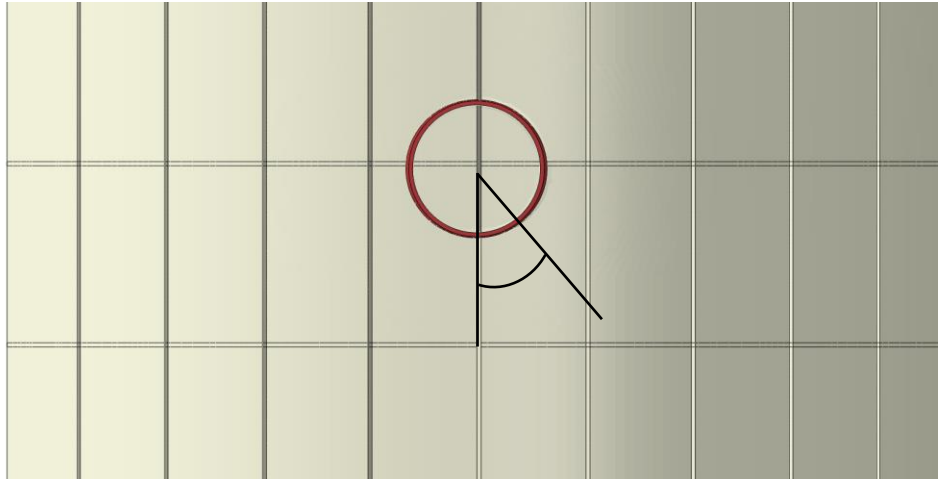
*Figure 41: Angle definition used for the SCF chart*

The Stress Concentration Factor on left and right side of the crown (±10 degrees) exhibits a maximum value of 3.5 while at the crown location (0 degrees) a minimum value of 1.8 because of the presence of stiffener.

## 5.6    Ultimate capacity of the joint

Besides the behavior of the joint in fatigue, the ultimate capacity is analyzed. The experimental results show that, the joint has an ultimate capacity of 208kN at 40mm displacement. Upon maximum value the reaction force diagram is dropping abruptly.

In both specimens, failure occurred at the crown of the primary brace-to-shell welded connection, on the shell side under tension, with significant rotation of the main brace member relatively to the shell surface. The crack extended progressively mainly along the weld circumference of the brace, and through the shell thickness until to a complete opening of the joint and fracture of the welded connection between the central stiffener and the shell underneath the crown position of the brace, as shown in Figure 42.



*Figure 42: Crack at P=209kN (peak load)*

The numerical model developed cannot indicate this drop in the reaction force, because it cannot model the process of fracture. However, it is interesting to observe the plastic deformations developed in the joint. As shown in Figure 43, plastic strain begins to develop at 7 mm displacement. The Reaction Force relationship begins to become nonlinear after the 7mm of displacement which is a clear indication that plastic strain develops.
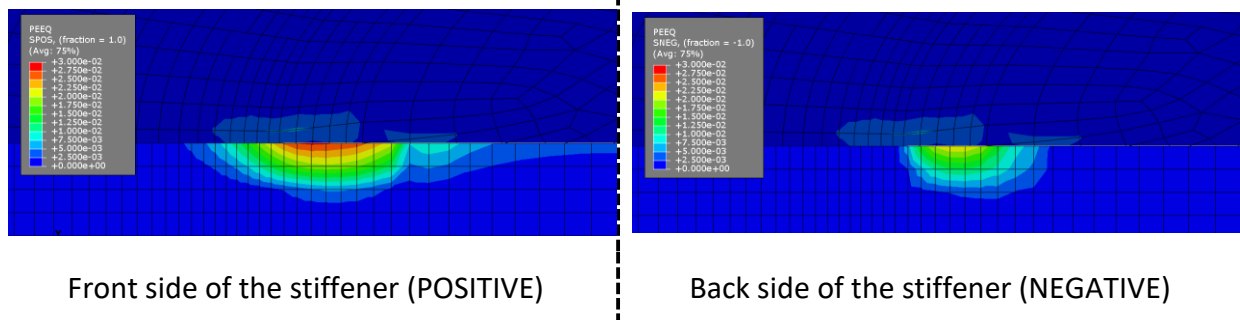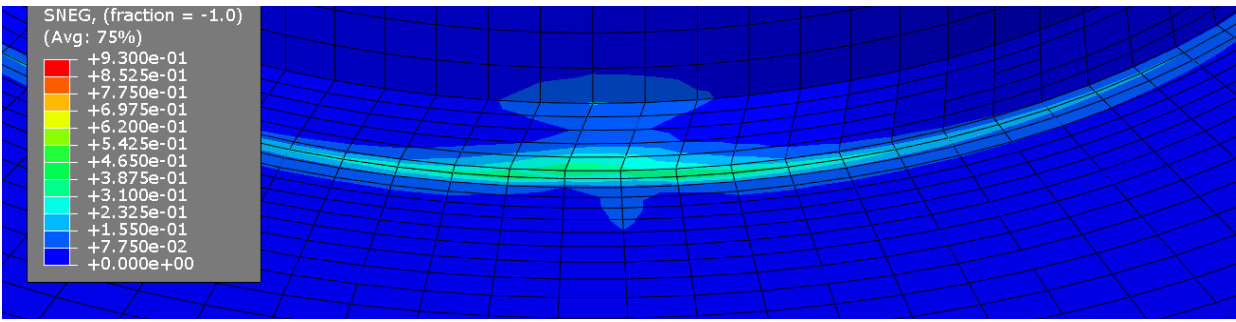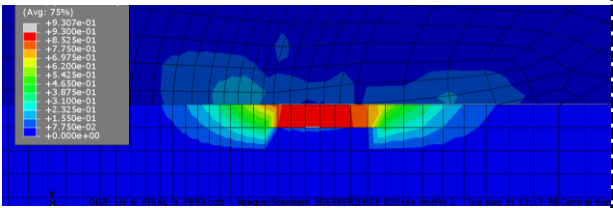


Plastic strain at the upper side of the skin, on the weld with the brace.
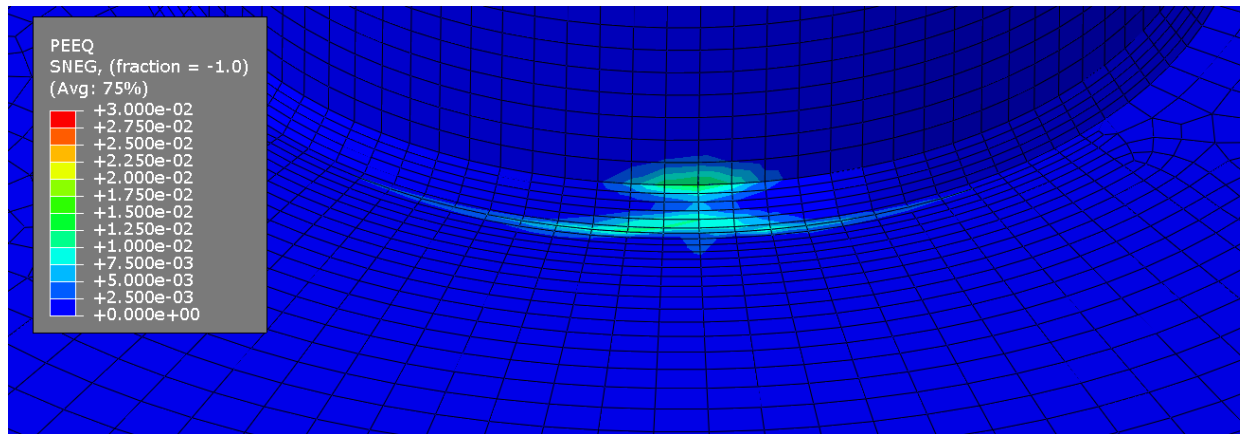


| Front side of the stiffener (POSITIVE) | Back side of the stiffener (NEGATIVE) |

*Figure 43: Plastic strains at 7mm displacement*

At the 45mm displacement, as shown in Figure 44, the plastic strain values at the stiffener side are larger compared to the upper skin side. This could be an indication that the stiffener broke first followed by the brace fracture from the skin. There is no indication that the crack initiated on the brace.

Plastic strain at the upper side of the skin, on the weld with the brace.
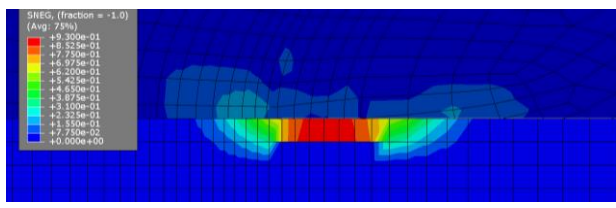


| Front side of the stiffener (POSITIVE) | Back side of the stiffener (NEGATIVE) |

*Figure 44: Plastic strains at 45mm displacement*

# 6 Alternative designs

According to the results and observations from the initial design, two designs are proposed for increasing the fatigue life and the ultimate capacity of the joint.

## 6.1 Proposed designs

The first proposed alternative design is shown in Figure 45. Four triangular plates have been placed at 30 degrees on the left and right side of both crown locations. The triangular plates are 250mm x 120mm.The thickness of the plates is 10mm.
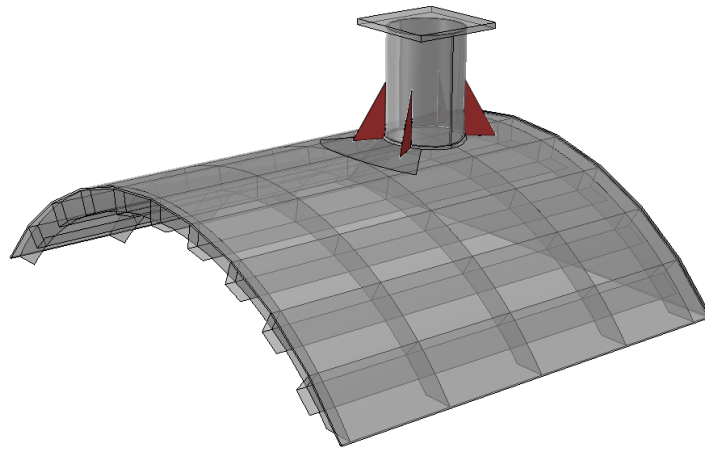


*Figure 45: Alternative design #1, triangular plates are shown in red color*

The second proposed alternative design is shown in Figure 46. An 8mm thick plate is placed above the skin and the brace is then welded on this reinforcing plate. The skin and plate are considered as one part, so no friction interaction is modelled between the two parts. The dimension of the plate is 600mm x 600mm.
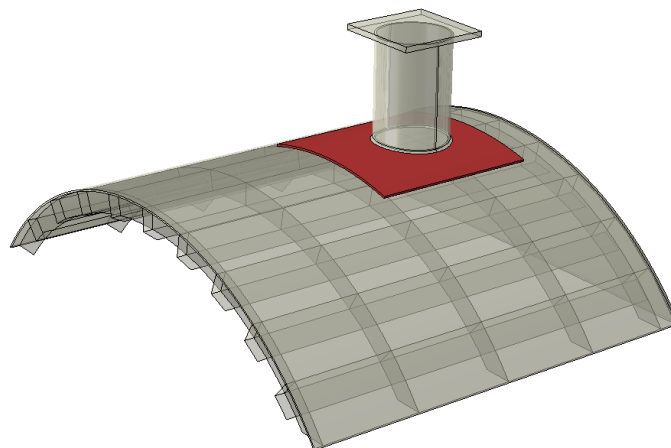


*Figure 46: Alternative design #2, reinforcing plate is shown in red color*

## 6.2    Reaction Force – Displacement diagram

The two designs are modelled and meshed in the same way with the initial design. The first criteria for evaluating the design are the Reaction Force – Displacement diagram. The diagram for each design is shown in Figure 47.

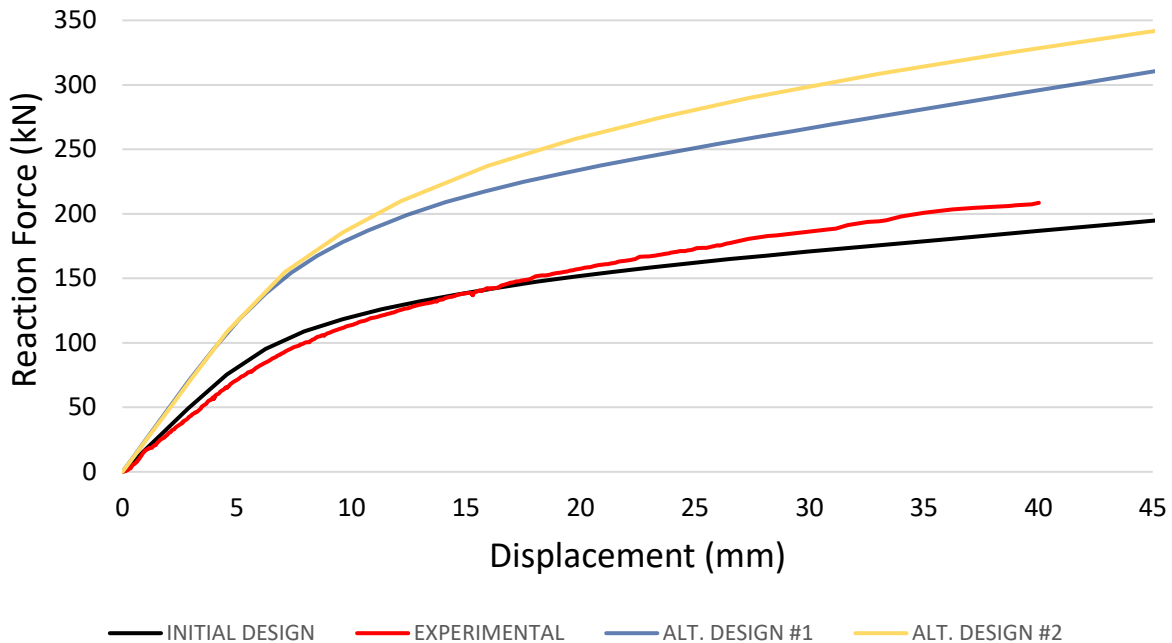The critical regions are going to analyzed next, comparing them with the initial design.



*Figure 47: Experimental, Initial design and alternative designs Reaction Force - Displacement diagram*

## 6.3    Designs comparison for fatigue

For evaluating the mechanical behavior of the alternative designs in fatigue, the stresses in two states are analyzed. The first state is P=27kN and the second P=90kN.

As shown in Figure 48, for both critical regions, the stress values developed in the alternative designs are lower compared to the stress values developed in the initial design. Again, the stress distribution in the stiffener is higher for both alternative designs. That means that any crack is more possible to initiate from the below "inner" side of the skin.

Comparing the two alternative designs, there is no significant difference regarding the two states.
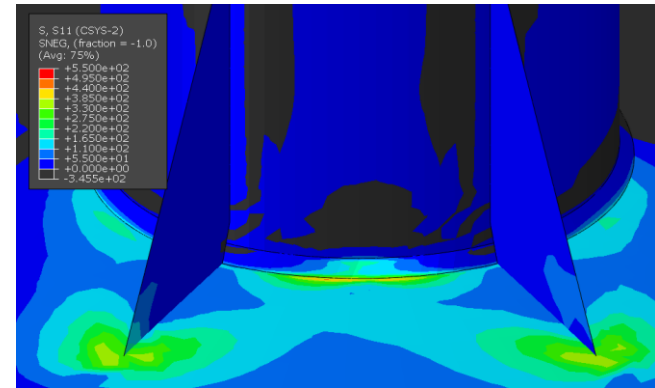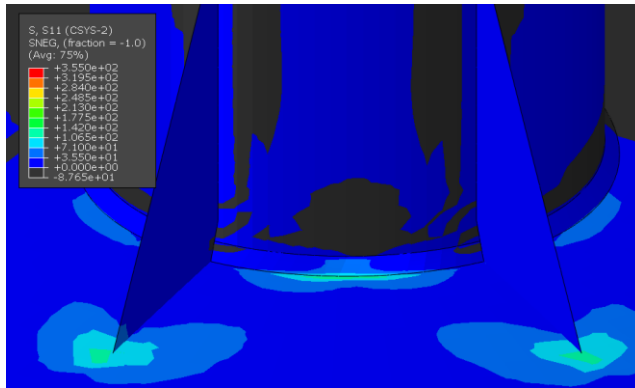
**P=27kN**                                                   **P=90kN**

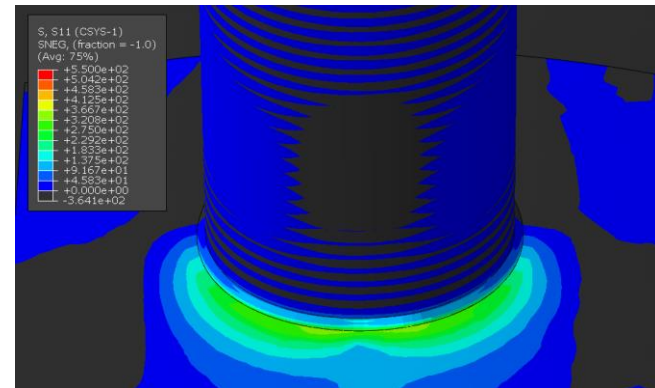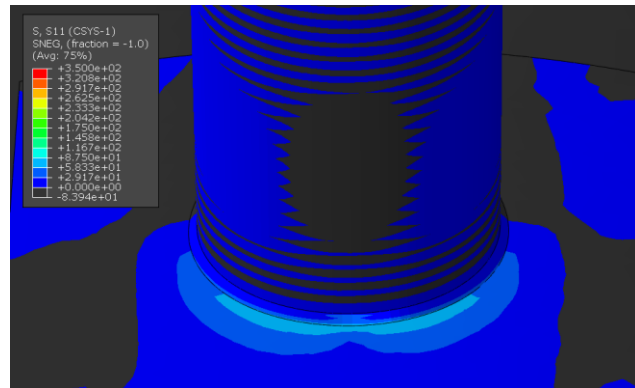**Initial design**
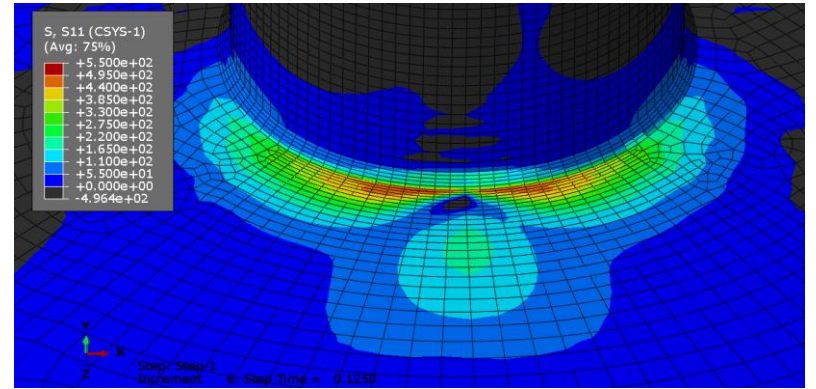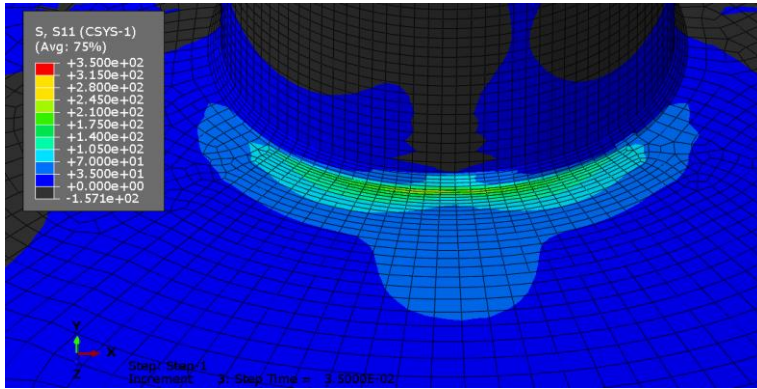
**Alt. design #1**
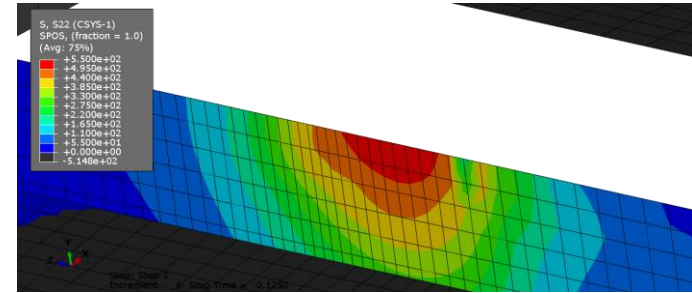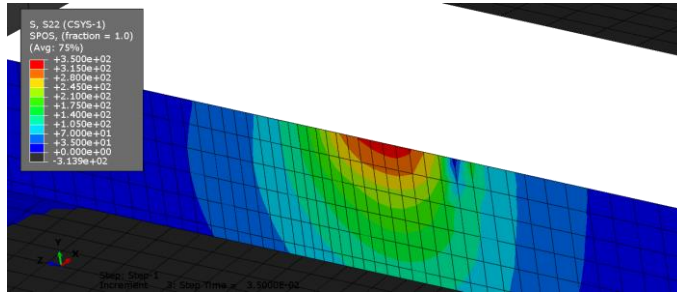
**Alt. design #2**
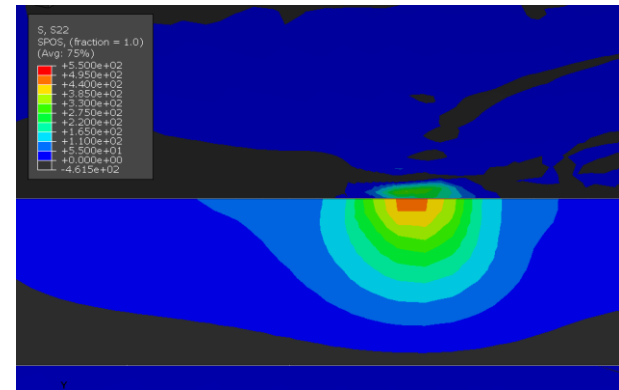
*Figure 48: Designs "upper" skin side stresses comparison*
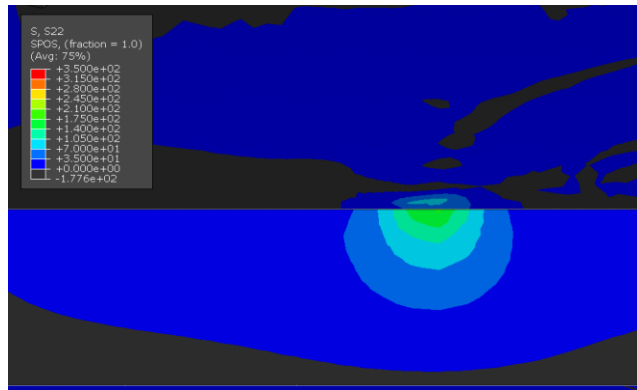
**P=27kN**

**P=90kN**

**Initial design**



**Alt. design #1**
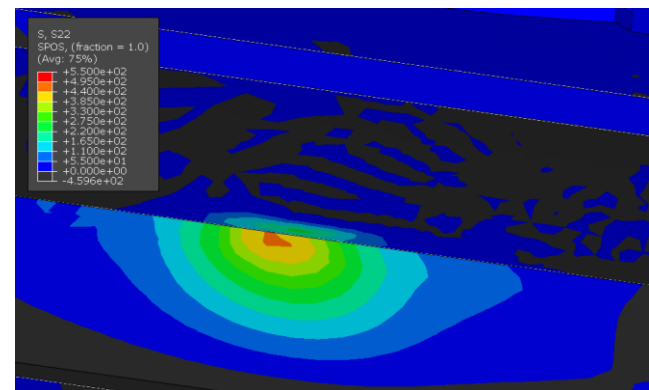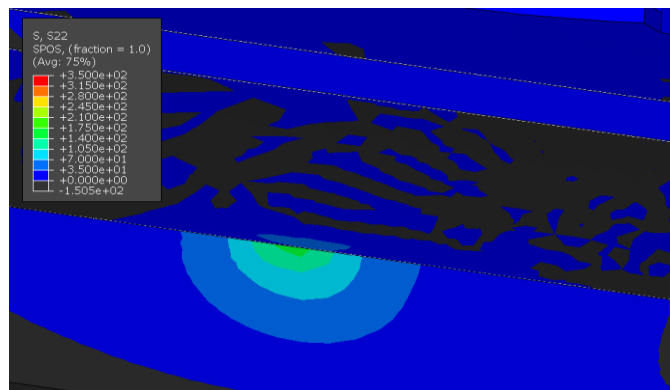


**Alt. design #2**



*Figure 49: Designs "inner" skin side and stiffener stresses comparison*

## 6.4    Designs comparison for ultimate joint capacity

It is obvious from Figure 47 that the alternative design #2 is improving the ultimate capacity of the joint. The alternative design #1 is improving the ultimate capacity by 54%, while the Alternative design #2 by 70%.

## 6.5    Further analysis of the alternative designs

Two conceptual alternative designs were analyzed. Their analysis needs attention, as both require a more detailed model and analysis.

For the alternative design #1, further analysis is needed in the tip of the triangular plates as high stresses are developed both on the brace and the skin. As this type of reinforcement is very common in marine structures, regulations about the stress concentration and design recommendations exist. Further analysis of this structure was not at the scope of this document. The critical regions on the skin are shown below in Figure 50.
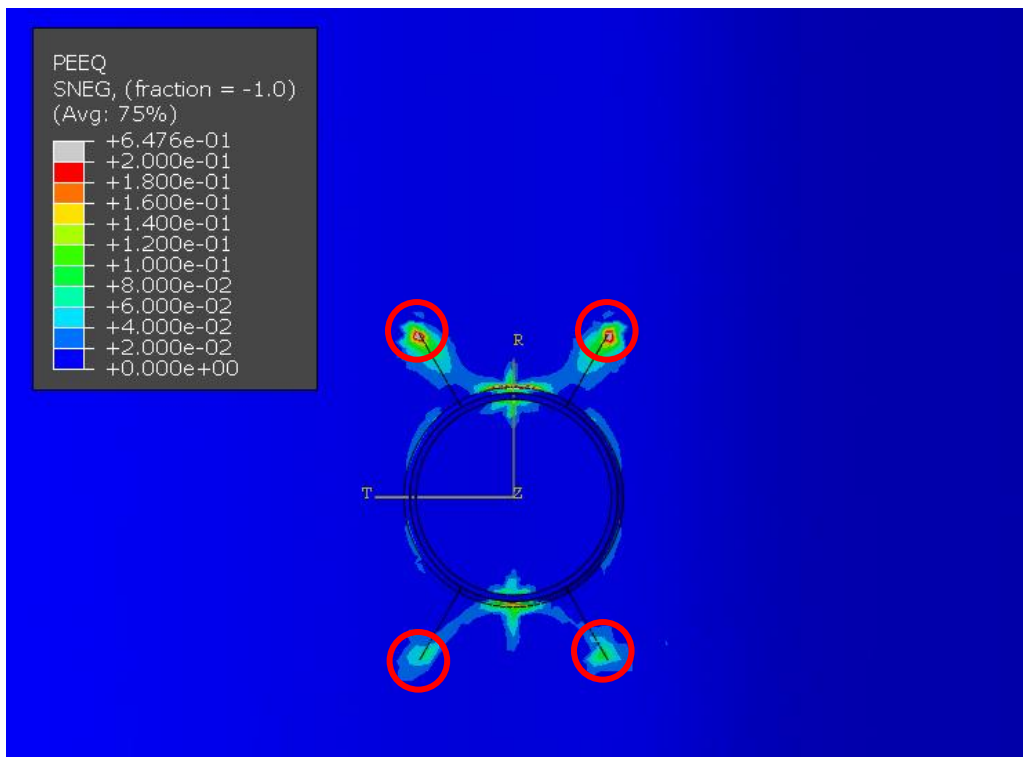


*Figure 50: Alternative design #1 high stress points*

For the alternative design #2, the 8mm reinforcing plate was merged with the skin. This simplification is not totally correct, as normally, the plate would be touching with the skin and welded on the perimeter. The correct modelling is shown in Figure 51. At the red continued line interface, the two faces should be tied (weldment). In the red dashed interface, the two faces should be touching, and friction interaction should be applied.
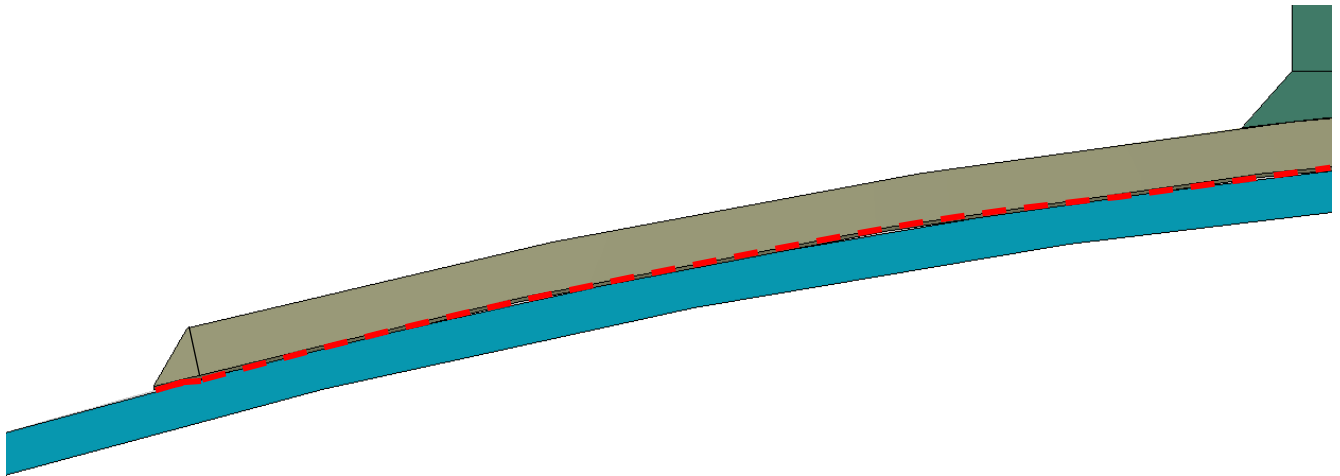
*Figure 51: Reinforcing plate - Skin interface at alternative design #2*

# 7  Summary and Conclusion

The mechanical behavior of a welded stiffened connection in a Tension Leg Platform (TLP) was presented in this thesis. No available data for Stress Concertation Factors (SCF) were available in the literature for this type of connection due to the low ratio of brace's diameter $d_1$ to chord's diameter $d_0$ and the reinforcing grid of stiffeners under the skin. For those reasons, a numerical model was developed for evaluating the mechanical behavior of the joint.

Some conclusions are discussed below, about the behavior of the connection in fatigue, the ultimate capacity of the connection and the alternative designs.

## 7.1  Fatigue Limit State Analysis

A through-thickness crack occurred at the crown position of the main brace-to-shell welded connection in all specimens under cyclic loading. Two critical points were detected for crack initiation; **(a)** the crown of the skin – brace weldment, at the upper side of the skin and **(b)** the stiffener – skin connection area at the "inner" side of the skin below the weldment crown. For low range load, below 45kN, the crack initiates from area **(b)**, propagates through the skin and leads to a through-thickness crack. For larger load ranges, the crack initiates from both areas **(a)** and **(b)**.

The numerical model presented has identified those two critical areas. The stresses developed on the "inner" side of the skin and the stiffener were higher, which confirms that the crack initiates from the inner side. In higher load ranges, the stress values are almost equal high in both areas.

## 7.2  Ultimate joint capacity

The ultimate capacity of the joint was calculated as well. The joint has a peak load of 209 kN at 40mm horizontal displacement. The numerical model underestimated the load at 40mm displacement, at 10%. Plastic strains are developed in both areas (a) and (b) after 7mm displacement. This point and then, the Reaction Force – Displacement curve is non-linear.

## 7.3  Alternative designs

According to the previous observations, two numerical modified designs were proposed; **(a)** one stiffened with four triangular brackets supporting the brace and **(b)** one reinforced with a rectangular plate, below the brace and above the skin. Both designs, are modeled with the same numerical setup as the initial design. Both had improved mechanical behavior in fatigue and higher ultimate capacity. In both cases some modelling techniques must be improved in future works for more precise results.